

Self-regulated AGN feedback of light jets in cool-core galaxy clusters

K. Ehlert^{1,2*}, R. Weinberger³, C. Pfrommer¹, R. Pakmor⁴, V. Springel⁴

¹*Leibniz Institute for Astrophysics, An der Sternwarte 16, D-14482 Potsdam, Germany*

²*Institut für Physik und Astronomie, Universität Potsdam, Karl-Liebknecht-Str. 24/25, 14476 Golm, Germany*

³*Canadian Institute for Theoretical Astrophysics, 60 St. George Street, Toronto, ON M5S 3H8, Canada*

⁴*Max-Planck-Institut für Astrophysik, Karl-Schwarzschild-Str. 1, D-85741 Garching, Germany*

Accepted XXX. Received YYY; in original form ZZZ

ABSTRACT

Heating from active galactic nuclei (AGN) is thought to stabilize cool-core clusters, limiting star formation and cooling flows. We employ radiative magneto-hydrodynamic (MHD) simulations to model light AGN jet feedback with different accretion modes (Bondi-Hoyle-Lyttleton and cold accretion) in an idealised Perseus-like cluster. Independent of the probed accretion model, accretion efficiency, jet density and resolution, the cluster self-regulates with central entropies and cooling times consistent with observed cool-core clusters in this non-cosmological setting. We find that increased jet efficiencies lead to more intermittent jet powers and enhanced star formation rates. Our fiducial low-density jets can easily be deflected by orbiting cold gaseous filaments, which redistributes angular momentum and leads to more extended cold gas distributions and isotropic bubble distributions. In comparison to our fiducial low momentum-density jets, high momentum-density jets heat less efficiently and enable the formation of a persistent cold-gas disc perpendicular to the jets that is centrally confined. Cavity luminosities measured from our simulations generally reflect the cooling luminosities of the intracluster medium (ICM) and correspond to averaged jet powers that are relatively insensitive to short periods of low-luminosity jet injection. Cold gas structures in our MHD simulations with low momentum-density jets generally show a variety of morphologies ranging from discy to very extended filamentary structures. In particular, magnetic fields are crucial to inhibit the formation of unrealistically massive cold gas discs by redistributing angular momentum between the hot and cold phases and by fostering the formation of elongated cold filaments that are supported by magnetic pressure.

Key words: methods: numerical – galaxies: clusters: intracluster medium – MHD – galaxies: jets – galaxies: active

1 INTRODUCTION

Cool-core (CC) clusters with central cooling times smaller than 1 Gyr form a subclass of galaxy clusters. However, the expected cooling flows are absent. Instead these clusters possess low star formation rates and low central entropies (Peterson & Fabian 2006). Jets driven by the central AGNs inflate buoyantly rising bubbles that are observed as X-ray cavities. The mechanical luminosity of AGNs estimated from cavity enthalpy appears to be tightly linked to the cooling luminosity (e.g., Birzan et al. 2004; Rafferty et al. 2006; Diehl et al. 2008), leaving sufficient heating energy to offset

the energy losses by the cooling ICM and establishing feedback from AGNs as the main heating source (McNamara & Nulsen 2012; Fabian 2012) in CC clusters.

The AGN is fueled by cooling gas accreted by the central super massive black hole (SMBH). The exact accretion mechanism remains uncertain. In many numerical simulations, Bondi-Hoyle-Lyttleton accretion (Bondi 1952; Hoyle & Lyttleton 1941) is employed due to its simplicity. However, observations find that Bondi accretion provides insufficient power to fuel active jets in clusters (e.g., Cavagnolo et al. 2011; McNamara et al. 2011; Russell et al. 2015; Fujita et al. 2016; Russell et al. 2018). The ICM is prone to the thermal instability, which acts when the cooling time t_{cool} is of order or shorter than the free fall time t_{ff} (Mc-

* E-mail: kehlert@aip.de

court et al. 2012). Cold gas may condense in the galaxy or can become thermally unstable as it is dragged up by the AGN (e.g., McNamara et al. 2016; Russell et al. 2017; Tremblay et al. 2018, but see, Jones et al. 2017). The condensing cold gas is then predicted to rain on the central SMBH as *cold accretion* (Pizzolato & Soker 2005; Sharma et al. 2012; Gaspari et al. 2017). Tremblay et al. (2016) report observational evidence of such a cold clumpy accretion flow towards a SMBH. In many CC clusters, cold gas takes a filamentary shape (e.g., Russell et al. 2019; Olivares et al. 2019) where clusters with low values of $t_{\text{cool}}/t_{\text{ff}}$ show more massive filaments (e.g., Cavagnolo et al. 2008; Voit & Donahue 2015; Lakhchaura et al. 2018 but see Martz et al. 2020).

Hydrodynamic simulations of galaxy clusters are able to produce a self-regulated feedback loop using a cold gas triggered SMBH accretion model which is coupled to the AGN feedback injection (e.g., Gaspari et al. 2012; Li & Bryan 2014; Prasad et al. 2015). However, there are various AGN jet models proposed in the literature that range from high-momentum density jets (with or without precession, Sternberg & Soker 2008; Hillel & Soker 2014, which heat mainly via mixing the cold and hot phases) to low-momentum density jets of various ICM-to-jet density ratios (Yang & Reynolds 2016; Weinberger et al. 2017; Beckmann & Dubois 2022), which can be more easily deflected by dense gas clouds in the path of propagation or by coherent and/or turbulent motions of the ambient ICM (Heinz et al. 2006).

When including star formation, Li et al. (2015) find a substantial suppression of the star formation rate compared to the expectation from an unmediated cooling flow for large enough efficiencies. A too low feedback efficiency, however, leads to high star formation rates $\gg 100 M_{\odot} \text{ yr}^{-1}$, inconsistent with observations (e.g., Fogarty et al. 2015). Cold gas properties are highly interconnected with the heating-cooling cycle: AGN-induced uplift is key in shaping the spatial distribution of cold gas (Yang et al. 2016), producing a wide range of cold gas cloud morphologies. Jets tend to shatter these structures (Beckmann et al. 2019). The addition of magnetic fields in simulations leads to a suppression of unrealistically massive cold gas discs that tend to appear in purely hydrodynamic simulations (Wang et al. 2021).

We simulate hot, low-density jets in an idealised magnetized CC cluster. In a companion paper (Weinberger et al., in prep.), we compare our low-density jet implementation to other AGN feedback implementations and study uncertainties arising due to resolution, parameter and model choices in detail. Here, we focus on (i) self-regulated feedback in CC clusters, and its dependence on the accretion prescription and jet properties, (ii) studying how mechanical X-ray cavity powers are related to the cooling luminosities and (simulated) jet luminosities, (iii) addressing the relevance of magnetic fields in redistributing the AGN feedback energy and in shaping the cold gas kinematics, and (iv) exploring how sensitive these results are to jet and accretion parameter choices.

The outline of our work is as follows. In Section 2, we describe our initial conditions and simulation setup. In Section 3 we demonstrate that independent of model choices, i.e. the adopted accretion model, probed jet efficiency and jet density, we obtain a self-regulated CC cluster. We analyse mechanical luminosities derived from X-ray cavities of our runs in Section 4 and study magnetic fields and the emerg-

ing cold gas in Section 5. We discuss our results in Section 6 and conclude in Section 7.

2 METHODS AND SIMULATION MODELS

We compute three-dimensional MHD simulations of AGN feedback in an idealised Perseus-like cluster with the moving-mesh code AREPO (Springel 2010; Pakmor et al. 2016). We use an HLLD Riemann solver (Pakmor et al. 2011; Pakmor & Springel 2013) with the Powell 8-wave scheme for magnetic divergence control (Powell et al. 1999). This solver has been shown to match several observed properties of magnetic fields in galaxies (Pakmor et al. 2017; Pakmor et al. 2018) and the circumgalactic medium (Pakmor et al. 2020). Moreover, the growth rates and saturation properties of the small-scale dynamo, the kinetic and magnetic power spectra, and statistics of magnetic curvature forces are in line with expectations from idealized turbulent box simulations of magnetic dynamos (Pfrommer et al. 2022), thus providing circumstantial evidence that our employed numerical method of moving mesh magneto-hydrodynamics with Powell cleaning delivers accurate results. In the following we describe the initial conditions, our ISM modeling, and further details of our jet/accretion models and simulation runs.

2.1 Initial conditions

We adopt the radial electron density profile from Churazov et al. (2003) rescaled to a cosmology with $h = 0.67$:

$$n_e = 46 \times 10^{-3} \left[1 + \left(\frac{r}{60 \text{ kpc}} \right)^2 \right]^{-1.8} \text{ cm}^{-3} + 4.7 \times 10^{-3} \left[1 + \left(\frac{r}{210 \text{ kpc}} \right)^2 \right]^{-0.87} \text{ cm}^{-3}, \quad (1)$$

which is set up in hydrostatic equilibrium with the gravitational potential comprised of an NFW cluster potential with virial radius $R_{200,\text{NFW}} = 2 \text{ Mpc}$, mass $M_{200,\text{NFW}} = 8 \times 10^{14} M_{\odot}$ and concentration parameter 5. On top of this cluster potential, we add a central galaxy potential approximated as an isothermal sphere with $M_{200,\text{ISO}} = 2.4 \times 10^{11} M_{\odot}$ with $R_{200,\text{ISO}} = 15 \text{ kpc}$ (Mathews et al. 2006). We only account for the gravity that results from a static background potential, neglecting effects of self-gravity. We confirmed that it has negligible effect in comparison runs.

The turbulent magnetic field is introduced as a Gaussian random field with a Kolmogorov slope on scales smaller than $k_{\text{inj}} = 37.5^{-1} \text{ kpc}^{-1}$ and white noise on larger scales. The chosen scale is consistent with observations (Vacca et al. 2018). We use a constant thermal-to-magnetic pressure ratio of $X_{B,\text{ICM}} = P_B/P_{\text{th}} = 0.0125$, lower than in previous work to reduce rather large resulting values of Faraday rotation measure (Ehlert et al. 2021). The initial mesh consists of three nested meshes, with increasing resolution towards the center. We used an iterative procedure to provide an initial magnetic field that obeys the magnetic divergence constraint, $\nabla \cdot \mathbf{B} = 0$. Details of the divergence-free field setup can be found in Ehlert et al. (2018).

We introduce temperature fluctuations in the initial

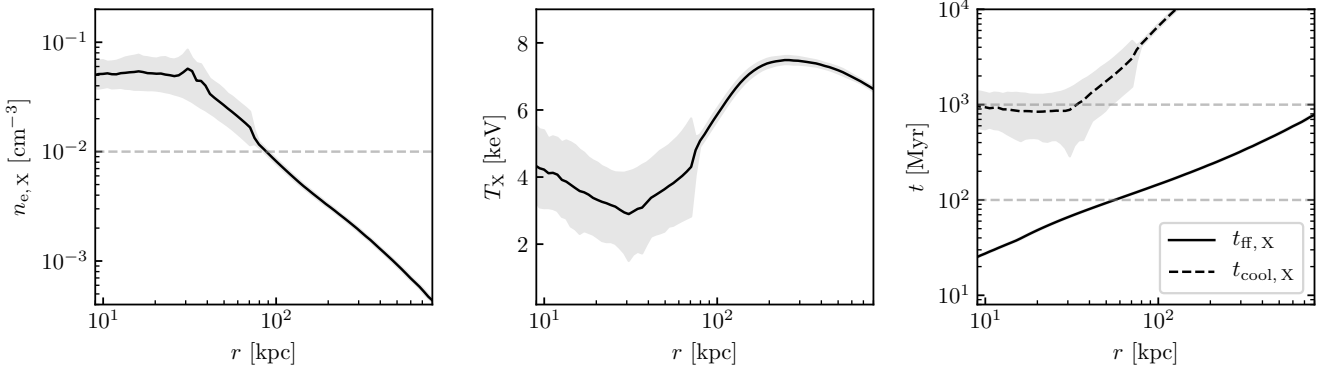


Figure 1. Radial profiles of the X-ray luminosity weighted electron number density (left), temperature (center), cooling time t_{cool} and free fall time t_{ff} (right) in our initial conditions. The shaded regions indicate the 10th and 90th percentiles. Only gas cells with $0.2 \text{ keV} < k_B T < 10 \text{ keV}$ are considered.

condition, seeding thermal instabilities at various stages to prevent the sudden emergence of a large amount of cold gas. We multiply the hydrostatic temperatures by values drawn from a Gaussian random field for $\delta T/T$ with dispersion $\sigma = 2$ and mean $\mu = 1$. The power spectrum of temperature fluctuations follows the Kolmogorov slope on scales smaller than $k_{\text{inj}} = 37.5^{-1} \text{ kpc}^{-1}$ and corresponds to white noise on larger scales, consistent with the power spectrum of the fluctuations in the magnetic field strength.

In addition, we seed velocity fluctuations in the central 800 kpc of the initial conditions to mimic orbiting substructures and random gas motions that result from gravitational potential rearrangements in the virialisation process. We initialize individual field components as a Gaussian random field with standard deviation $\sigma = 70 \text{ km s}^{-1}$. Powers on other scales are set to zero. The history of the initial velocity field is quickly erased as the jet significantly perturbs the velocity field within the crucial inner 200 kpc. Note, we use the same velocity fluctuations for all simulations analysed to simplify comparison across the different simulations.

In order to ease comparison to X-ray observations, we weight some quantities with the cooling luminosity of the X-ray emitting gas cells. Here, we only include cells with temperatures $0.2 \text{ keV} < k_B T < 10 \text{ keV}$. The cooling luminosity is directly taken from the simulation. We refer to this weighting scheme as “X-ray luminosity weighted” in the following. In Fig. 1, we show radial profiles of the X-ray luminosity weighted electron number density, temperature, cooling time t_{cool} and free fall time t_{ff} .

The free-fall time t_{ff} (Sharma et al. 2012) (or *local dynamical time*, Mccourt et al. 2012) is given by

$$t_{\text{ff}} = \sqrt{2r/g} \quad (2)$$

where $g = d\Phi/dr$ corresponds to the local acceleration due to gravity. The cooling time is defined via

$$t_{\text{cool}} = \frac{\varepsilon_{\text{th}}}{\dot{\varepsilon}_{\text{cool}}}, \quad (3)$$

where ε_{th} is the thermal energy density and $\dot{\varepsilon}_{\text{cool}}$ is the cooling luminosity for X-ray emitting gas (with $0.2 \text{ keV} < k_B T < 10 \text{ keV}$) in our simulations. Figure 1 shows that the Gaussian temperature fluctuations introduce cells that start condens-

ing soon after the start of the simulations while more than 90 per cent of the gas has cooling times exceeding 300 Myrs.

2.2 Cooling and star formation

The modeling of cooling, star formation and stellar feedback follows Vogelsberger et al. (2013) with updates and parameter choices consistent with the IllustrisTNG model (Pillepich et al. 2018). Cooling is modeled down to temperatures of 10^4 K using primordial and metal-line cooling assuming a constant metallicity of 0.3 times the solar value, which is motivated by an observed uniform ICM iron abundance $Z_{\text{Fe}} \approx 0.3$ in solar units (Werner et al. 2013) for $r \lesssim 1.5 \text{ Mpc}$. Treatment of star formation and supernova feedback are part of the ISM model described in Springel & Hernquist (2003). The model implements star formation as a stochastic process, where the star formation probability is tied to the free fall time of the gas and calibrated to follow the observed Kennicutt relation (Kennicutt 1998). Supernovae feedback heats the hot ICM and evaporates cold clouds. This leads to a tightly regulated regime for star formation. In the model this translates to an ISM that is pressurized by star formation feedback such that cold and hot phase coexist in pressure equilibrium, with the pressure given by a density dependent effective equation of state (eEOS). Above a density threshold of $n_e = 0.13 \text{ cm}^{-3}$, gas can exist either on this effective equation of state (see red line in Fig. 2) and form stars or as non star-forming phase with larger temperatures, but not below it. Gas on this eEOS is by definition star forming and, as mentioned in the previous subsection, also the main fuel for SMBH accretion. Stellar feedback beyond that implicitly accounted for by the eEOS is not modeled. At the chosen halo mass scale these stellar feedback effects are anyhow subdominant.

2.3 Jet

Provided the AGN cavities are in pressure equilibrium with the ambient ICM and supported by (entrained) thermal plasma (Croston & Hardcastle 2014; Croston et al. 2018), the X-ray surface brightness maps imply a low cavity density and constrain this gas to be much hotter than the sur-

rounding ICM. Because the bright X-ray emission of the ICM along the line of sight is projected onto the potentially faint emission from the cavities, X-ray spectroscopy alone is unable to probe the existence of very hot diffuse thermal plasma in excess of tens of keV filling the cavities. In fact, the high cavity-to-ICM density contrast was used to constrain the temperature of thermal plasma potentially supporting the cavities to $k_B T > 20\text{--}50$ keV (Nulsen et al. 2002; Blanton et al. 2003; Sanders & Fabian 2007).

Instead, a thermally supported cavity provides a Sunyaev-Zel'dovich (SZ) signal that is distinguishable from the signal of a cavity supported by magnetic fields and non-thermal relativistic particles, which themselves contribute minimally to the SZ effect (Pfrommer et al. 2005; Ehlert et al. 2019). Observations of the Sunyaev-Zel'dovich Effect in MS 0735.6+7421 show a clear deficit in signal consistent with temperatures of $\gtrsim 1000$ keV in the case of thermal pressure supported bubbles (Abdulla et al. 2019). This corresponds to an ICM-to-jet density contrast of $\rho_{\text{ICM}}/\rho_{\text{jet}} > 10^2$ to 2×10^2 (and likely much larger). We therefore adopt $\rho_{\text{jet}} = 10^{-28} \text{ g cm}^{-3}$ (i.e., $\rho_{\text{ICM}}/\rho_{\text{jet}} \sim 3 \times 10^3\text{--}10^4$) as our fiducial jet density. Jets are injected in a bi-directional fashion with zero opening angle from a spherical region with radius $r = r_{\text{acc}}/3$ (Weinberger et al., in prep.). We inject a helical magnetic field in the jet fluid with a magnetic-to-thermal pressure ratio $X_{B,\text{jet}}$.

Talbot et al. (2021) model accretion of geometrically thin discs and launch jets using the Blandford & Znajek (1977) model. They find that the jet direction varies mildly by 25° over 10 Myr for the most extreme case, when the jet is launched into the accretion disc, while it remains stable otherwise. Lower black hole-spin values lead to a more efficient reorientation of the spin (Beckmann et al. 2019), because only little accreted material (with a different spin) is needed to torque the SMBH spin while maximally spinning Kerr black holes require the accretion of at least the mass of the black hole itself to change the spin orientation by unity. Realistic accretion models require the modeling of a geometrically thick disc in the low-Eddington accretion regime as expected for jets. This implies turbulent discs in which the magnetorotational instability can transport angular momentum to larger radii, thus limiting the accreted angular momentum and black-hole spin reorientation, which has a direct consequence on the jet launching direction. Importantly, chaotic cold accretion implies the feeding of the accretion disc with material of random angular momentum, such that the average angular momentum does not appreciably change over time scales of 1 Gyr, which justifies our choice of a steady jet direction. Similar theoretical arguments have been made by Nixon & King (2013), suggesting that rapidly reorienting jets would be an indication against a Blandford-Znajek jet launching mechanism.

To set up the jet state, we select gas cells within a spherical region with radius $r = r_{\text{acc}}/3$ and set their density to the pre-defined value ρ_{jet} . Unlike in previous studies (Weinberger et al. 2017), this is done directly in the center and the mass that is removed from (or added to) this jet region is not redistributed to the surroundings, but added to the gravitating mass of the black hole, ensuring total mass conservation. This mass is treated as a reservoir for future accreted gas in the black hole accretion routine. The total energy in the system is reduced by $\Delta m \langle u \rangle$, where Δm is the

mass change and $\langle u \rangle$ is the ambient specific thermal energy. The gas cells in the spherical shell outside the jet region but within a radius of r_{acc} are used to determine these ambient gas properties. In the jet region, we add internal energy to ensure that cells are at least in pressure equilibrium with the surroundings. Note that we do not allow for internal energy to be reduced at this step. From the jet energy available at a timestep, $L_{\text{jet}} dt$, we subtract the energy required to set up the jet state with its fixed density and in pressure equilibrium with its surroundings and inject the remaining energy in the form of kinetic energy bidirectionally without opening angle into the jet region. To trace the jet, we initialize a passive scalar $X_{\text{jet}} = 1$ in the jet region and advect it with the fluid. Our target mass is based on distance from the centre as

$$m_{\text{target}} = m_{\text{target},0} \exp(r/100 \text{ kpc}), \quad (4)$$

with cells at the outskirts limited to a maximum volume with a cell radius $r_{\text{cell}} = 370$ kpc. To sustain the strong density gradient between jet and ICM, we additionally refine cells with $X_{\text{jet}} > 10^{-3}$ to a target volume $V_{\text{jet,target}}$, where we limit the volume ratio between neighboring cells to 4 (see Weinberger et al. 2017, and Weinberger et al., in prep. for further details on the jet implementation). Table 1 shows the corresponding values for the discussed parameters in our runs.

2.4 Accretion

One focus of this study is to analyse the impact of the employed accretion model. Here, we use Bondi accretion and chaotic cold accretion with implementation details presented in the following. For the accretion rate estimate we use gas properties from cells within radius r_{acc} from the SMBH (excluding the jet region). We assume an initial black hole mass of $4 \times 10^9 M_\odot$, in rough agreement with expectations from black hole-halo scaling relations. This is an order of magnitude more massive than the SMBH in NGC1275 in the center of the Perseus cluster (Wilman et al. 2005; Scharwächter et al. 2013), which is an outlier in the black hole - host scaling relations (Sani et al. 2018).

2.4.1 Cold accretion

We parameterize the SMBH accretion rate \dot{M} in the cold mode as

$$\dot{M}_{\text{cold}} = \epsilon \frac{M_{\text{cold}}}{t_{\text{ff}}}, \quad (5)$$

where M_{cold} includes star forming gas and gas with a temperature below 2×10^4 K. Note, M_{cold} corresponds to the total gas mass of the cell. We do not explicitly compute the mass component of the cold phase in the ISM model. We then drain mass $\Delta M_{\text{bh},i} = \dot{M}_{\text{cold},i} \Delta t$ from all cold gas cells i during timestep Δt and increment the black hole mass by the total drained gas mass $\sum_i \Delta M_{\text{bh},i}$. When calculating the free-fall time t_{ff} , we only consider gravitational acceleration due to the static galaxy and cluster potential.

Not all gas arrives at the BH within t_{ff} due to the angular momentum of the gas. Processes that lead to angular momentum cancellation, e.g. cloud collisions (Gaspari et al.

2017), are not necessarily efficient enough under all circumstances. In addition, unresolved small-scale feedback may evaporate a fractions of the cold gas. To take these effects into account, we introduce the parameter $\epsilon < 1$ which represents a simple parametrization of the importance of these effects. Due to the high pressure environment of a massive galaxy cluster, our temperature threshold is below the effective temperature of most cold gas given by the effective equation of state of the interstellar medium (ISM, Springel & Hernquist 2003, see Fig. 2). Therefore the SMBH is default mostly accreting gas from the star forming phase.

The jet power L_{jet} is proportional to a fraction η of the accreted rest-mass energy

$$L_{\text{jet}} = \eta \dot{M}_{\text{cold}} c^2 = \eta \epsilon \frac{M_{\text{cold}}}{t_{\text{ff}}} c^2, \quad (6)$$

where c denotes the speed of light.

2.4.2 Bondi accretion

We compare the cold gas based accretion model to the frequently used Bondi accretion estimate. The Bondi accretion rate is given by

$$\dot{M}_{\text{bondi}} = \frac{4\pi G^2 M^2 \rho}{c_s^3}, \quad (7)$$

where M is the SMBH mass, c_s is the speed of sound, ρ is the mass density of the accreting medium. Assuming spherical accretion, the accretion rate must be below the Eddington limit. In practice, this limit is never reached in our runs. Analogously to cold accretion, the jet power is given by

$$L_{\text{jet}} = \eta \dot{M}_{\text{bondi}} c^2. \quad (8)$$

2.5 Simulation runs

Simulations discussed in the following are summarized in Table 1. The **Fiducial** model uses cold accretion with our fiducial efficiency parameters $\epsilon = 0.1$ and $\eta = 0.01$. To study the impact of magnetic fields, we rerun **Fiducial** by excluding MHD, which we call **HD**. Our **Bondi** run with fiducial Bondi accretion allows comparisons with a different mode of accretion. We analyse effects of numerical resolution by rerunning **Fiducial**, **HD** and **Bondi** at 10 times higher mass resolution, reduced accretion radius $r_{\text{acc}} = 1$ kpc and a factor of 2 higher spatial resolution in the jet (see Table 1). We refer to the high resolution runs as **HR**, **HDHR** and **BondiHR**, respectively. We also vary the efficiency parameters ϵ and η of the cold accretion model and increase the jet density by 10^3 in our **Dense** model. To assess the effects of our jet feedback, we remove the SMBH and its associated feedback in run **NoBH**.

3 A SELF-REGULATED COOL-CORE CLUSTER

We first focus on the state of self-regulation seen in our simulations. The time evolutions of the different models are exemplified in Fig. 3, where we show density and entropy slices, the surface density of the gas with a cooling time below 30 Myr and the X-ray emissivity of gas with $0.2 \text{ keV} < k_B T < 10 \text{ keV}$ of our **HR** model ($\epsilon = 0.1$, $\eta = 0.01$,

cold accretion). Low density jets inflate cavities with density contrasts of $\sim 10^4$ that rise buoyantly in the cluster atmosphere.¹ Cluster weather resulting from turbulent intracluster motions deflects bubbles throughout the run. Additionally, central cold gas deflects the forming bubbles early which leads to more isotropised feedback. Deflection of bubbles by cluster weather and cold gas is seen in many simulations (e.g., Sijacki et al. 2008; Morsony et al. 2010; Mendygral et al. 2012; Bourne & Sijacki 2017; Bourne et al. 2019). The gas in the wake of bubbles experiences a strong uplift, which advects low-entropy gas from the center to larger radii so that the upwards path leading to the high-entropy bubbles is traced by low-entropy gas that originates from the center (as discussed in Chen et al. 2019; Ehlert et al. 2021; Zhang et al. 2022). Gas with low cooling time accumulates in the center and forms filamentary structures and/or transient discs (e.g. at 1600 Myr). The bubbles are clearly discernible as high-contrast cavities in the X-ray emissivity.

In Fig. 2, we show a phase diagram of temperature T vs. electron number density n_e when the jet is inactive (left) and active (right) in the central 100 kpc of the cluster. As our low-density jets are set up in pressure equilibrium with the surrounding ICM, the jets are comprised of hot, low-density gas. Interestingly, the ICM pressure in the cluster center only varies by roughly an order of magnitude. This implies that jet feedback does not create any dramatically over-pressured gas in galaxy clusters, which, in turn, would cause strong shocks (see the parameter study in Ehlert et al. 2018). Cooling gas moves isobarically onto the effective equation of state (eEOS) where it forms stars. Further cooling to higher densities and lower temperatures is limited by the eEOS.

We study the long-term impact of AGN feedback on the ICM in Fig. 4, where we show radial profiles of the X-ray weighted ($0.2 \text{ keV} < k_B T < 10 \text{ keV}$) density $n_{e, X}$, temperature T_X , entropy K_X and thermal pressure $P_{\text{th}, X}$ of various runs. Dashed lines separate strong CC clusters from moderate CC/non CC clusters as observationally determined (Cavagnolo et al. 2008; Hudson et al. 2010). Central densities remain high throughout time independent of accretion model, resolution and jet density, well above the CC limit. The initialization of denser jets in our **Dense** model lead to even higher densities in this run. Generally, the central entropy stays well below 10 keV cm^2 . As noted previously, radiative cooling of our initial conditions causes the central temperature to drop by a factor of ~ 3 , the density to increase by a factor of a few and therefore the entropy to decrease by a factor ~ 10 .

Interestingly, the cluster self-regulates at these new equilibrium profiles throughout the runtime of the simulation, implying that our AGN jet feedback stabilises the system but cannot substantially alter the thermodynamic profile of our CC galaxy cluster or even transform it into

¹ While the central electron number density in the initial conditions is $5 \times 10^{-2} \text{ cm}^{-3}$ (Eq. 1), successive cooling and compression increases the central electron density so that it self-regulates around a new equilibrium profile with central densities of ~ 0.3 – 1 cm^{-3} (see Fig. 4), which implies ICM-to-jet density contrasts of $\sim 3 \times 10^3$ – 10^4 in our fiducial low-density jets (and ~ 10 in our **Dense** model) at jet launching.

Label	accretion	ϵ	η	ρ_{jet} [g cm ⁻³]	$m_{\text{target},0}$ [10 ⁵ M _⊙]	$V_{\text{jet,target}}^{1/3}$ [kpc]	r_{acc} [kpc]	radiative cooling	$X_{B,\text{ICM}}$	$X_{B,\text{jet}}$
Fiducial	cc	0.1	0.01	10 ⁻²⁸	15	0.65	2	✓	0.0125	0.1
Dense	cc	0.1	0.01	10 ⁻²⁵	15	0.65	2	✓	0.0125	0.1
HD	cc	0.1	0.01	10 ⁻²⁸	15	0.65	2	✓	0	0
Bondi	bo	-	0.01	10 ⁻²⁸	15	0.65	2	✓	0.0125	0.1
NoBH	-	-	-	-	15	-	-	✓	0.0125	-
NoBHNoCool	-	-	-	-	15	-	-	-	0.0125	-
HR	cc	0.1	0.01	10 ⁻²⁸	1.5	0.3	1	✓	0.0125	0.1
HDHR	cc	0.1	0.01	10 ⁻²⁸	1.5	0.3	1	✓	0	0
BondiHR	bo	-	0.01	10 ⁻²⁸	1.5	0.3	1	✓	0.0125	0.1
Varying accretion parameters										
	cc	0.1	0.1	10 ⁻²⁸	15	0.65	2	✓	0.0125	0.1
	cc	0.01	0.01	10 ⁻²⁸	15	0.65	2	✓	0.0125	0.1
	cc	0.01	0.001	10 ⁻²⁸	15	0.65	2	✓	0.0125	0.1
	cc	1	0.0001	10 ⁻²⁸	15	0.65	2	✓	0.0125	0.1
	bo	-	0.001	10 ⁻²⁸	15	0.65	2	✓	0.0125	0.1

Table 1. Simulation parameters with accretion model (bo for Bondi accretion, and cc for chaotic cold accretion), efficiency parameters ϵ and η , jet density ρ_{jet} , target mass $m_{\text{target},0}$, jet target volume $V_{\text{jet,target}}$, radius of accretion region r_{acc} , thermal-to-magnetic pressure ratio in the ICM $X_{B,\text{ICM}}$ and in the jet $X_{B,\text{jet}}$.

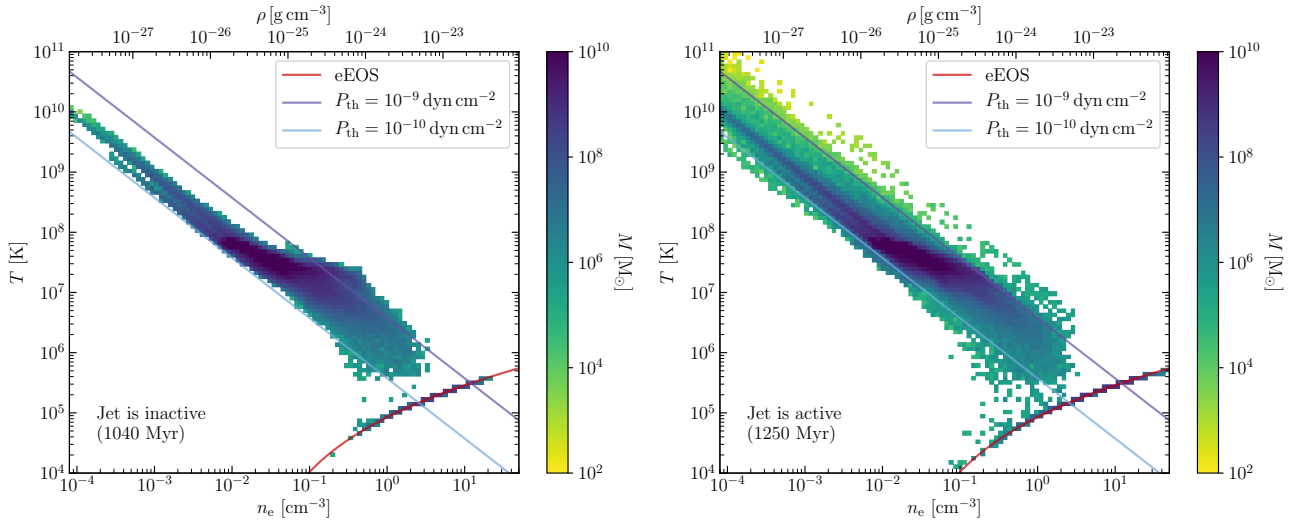


Figure 2. Phase diagram of the electron number density n_e and temperature in the central 100 kpc at 1040 Myr (where the jet is inactive) and at 1250 Myr (where the jet is active) in the run **Fiducial**. Color coding corresponds to total mass in respective bins. The effective model of the ISM inhibits cooling below the effective equation of state (red line). The plasma is near pressure equilibrium. Lines of constant pressure are shown in blue and purple.

a non-CC cluster (in agreement with the statistics of observed AGN bubble enthalpies and central ICM entropies, Pfrommer et al. 2012). For comparison, we show profiles for model **NoBH** at 1200 Myr in the second column of Fig. 4, which enters a run-away cooling state with a dense cold core that causes SFRs elevated by nearly two orders of magnitude over the other models. More work with different initial conditions and cosmological settings is needed to test the universality of this prediction. Increasing the initial density and introducing a more granulated density structure as seen in turbulent box simulations (e.g., Mohapatra et al. 2021) may lead to equilibrium densities at the observed levels (see Eq. (1), Churazov et al. 2003).

To explore the cooling gas, we show in Fig. 5 radial profiles of X-ray weighted ($0.2 \text{ keV} < k_B T < 10 \text{ keV}$) cooling time $t_{\text{cool},X}$ and the cooling-to-free fall time ratio $[t_{\text{cool}}/t_{\text{ff}}]_X$. In addition, we plot the total mass per logarithmic bin, $[dM/d \log(r)]_{<100 \text{ Myr, No SF}}$, for non-star-forming gas with $t_{\text{cool}} < 100 \text{ Myr}$. The cooling times stay below 1 Gyr within the inner 50 kpc independent of the accretion model, resolution and jet density. The cooling-to-free fall time ratio remains low within $r \lesssim 50 \text{ kpc}$ at $[t_{\text{cool}}/t_{\text{ff}}]_X < 10$. For $t > 400 \text{ Myr}$ cold gas is present in the center at $r \lesssim 30 \text{ kpc}$. This state of cooling appears to be a general feature of our simulations.

In Fig. 6, we show the time evolution of the cold gas

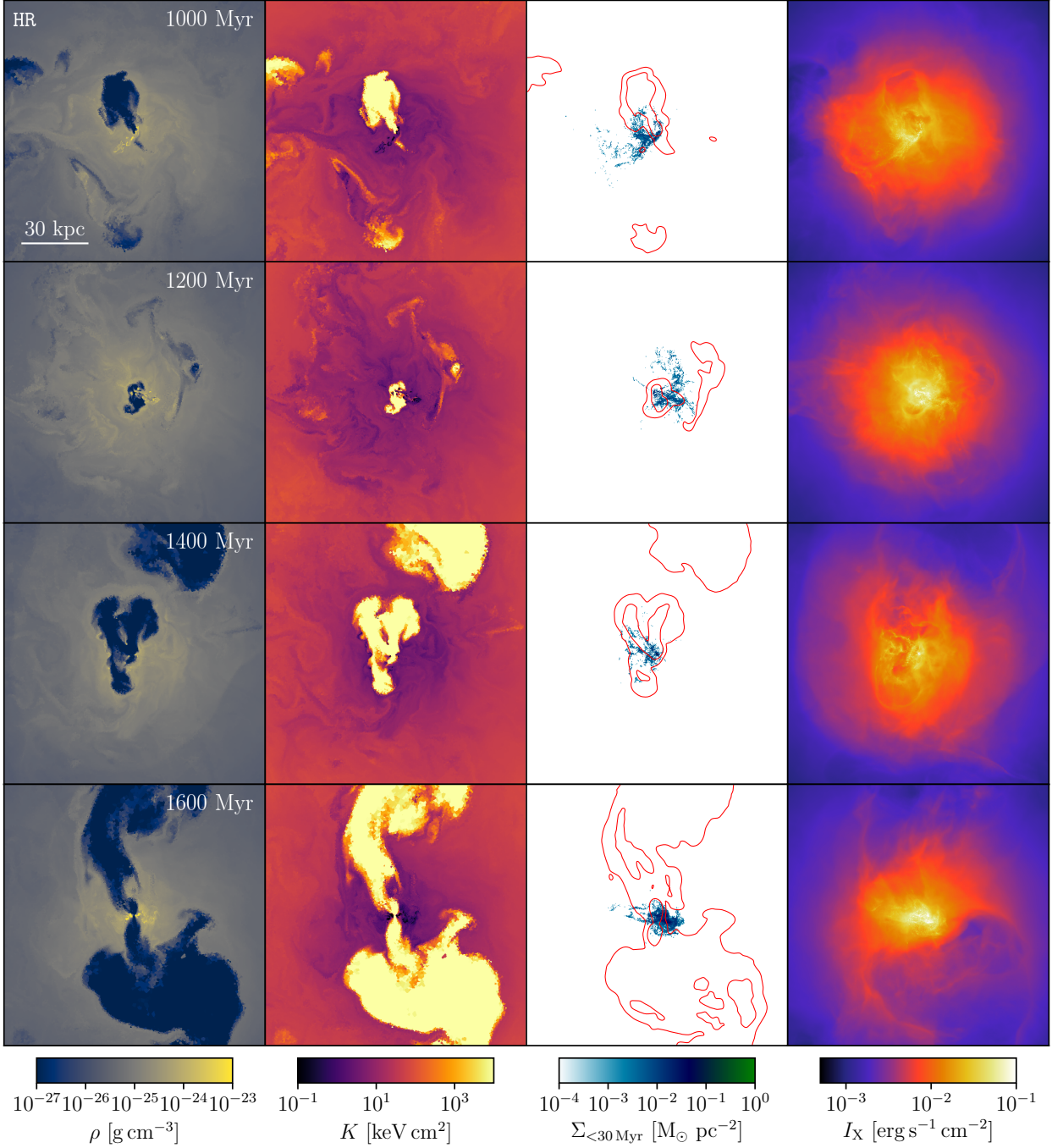


Figure 3. Overview of the fiducial high resolution cold accretion simulation HR (with accretion parameters $\epsilon = 0.1$ and $\eta = 0.01$). We show thin slices of side length 120 kpc of the mass density ρ , entropy $K = k_B T n_e^{-2/3}$, cold gas surface density $\Sigma_{<30\text{Myr}}$ where $t_{\text{cool}} < 30\text{Myr}$ and the X-ray emissivity I_X is in the Chandra band (for which we adopt our simulated cooling luminosity that includes metal line cooling). Cold gas deflects the jet which allows it to heat the cooling ICM more isotropically. High entropy gas is only found in the bubbles, whereas the bulk of the ICM remains at low entropy typical for CC clusters.

mass (M_{cold} with $T < 10^6\text{K}$), the star formation rate (SFR), the jet luminosity (L_{jet}) and the SMBH mass (M_{bh}). Due to the Gaussian temperature fluctuations in the initial conditions, cold gas collapses in multiple clumps at $r \sim 20\text{kpc}$. The clumps fall towards the center but due to their angular momentum, they overshoot in their orbits. Initial SMBH accretion is thus limited to short bursts when the

clumps pass near the SMBH. After $\sim 500\text{Myr}$, our AGN jet feedback establishes a cycle of self-regulation on characteristic timescales throughout individual runs with similar jet powers and SFRs for each run. Therefore, we focus our analysis on times after 500 Myr. SFRs are closely tied to cold gas formation. Runs including AGN jet feedback show $\text{SFR} \sim 10 M_{\odot} \text{yr}^{-1}$ while our NoBH model reaches

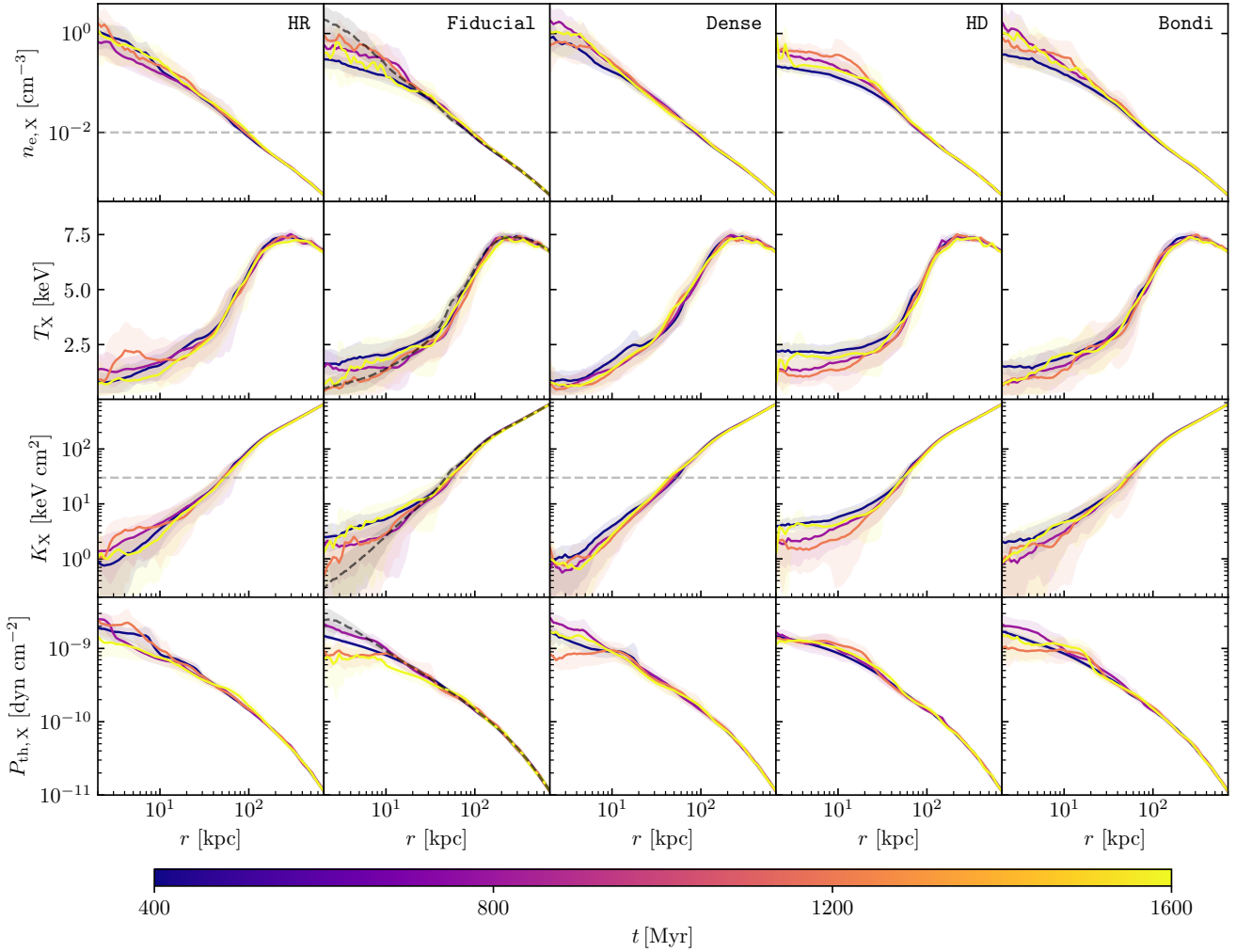


Figure 4. Radial profiles of the X-ray weighted density $n_{e,X}$, temperature T_X , entropy K_X and thermal pressure $P_{th,X}$. The different colours correspond to simulation times as indicated on the colour bar. Profiles for model NoBH at 1200 Myr are shown in dashed in the second column. Shaded areas indicate the 10th to 90th percentiles and dashed lines represent popular choices for defining CC clusters (with central densities above 10^{-2} cm⁻³ and central entropies less than 30 keVcm²). A self-regulated heating-cooling cycle leads to a dynamical attractor solution resembling that of observed CC clusters irrespective of the accretion mode and for all probed parameters.

SFR $> 400 M_{\odot} \text{ yr}^{-1}$. The **Dense** model shows systematically larger SMBH accretion rates. The increased accretion rates imply larger SMBH masses and AGN jet luminosities (by a factor of ~ 2 , see dashed lines in Fig. 6) so that the SFR is more quenched in comparison to the other models. As we will show below, this model enables the formation of long-lived discs that continuously feed the SMBH.

For runs including jet feedback, the cold gas masses mostly stay in the range $10^9 M_{\odot} < M_{\text{cold}} < 10^{10} M_{\odot}$ after $t > 500$ yr. Only the model NoBH forms significantly more cold gas, which implies a substantially increased SFR. Towards the end of our HD simulation, we observe a large amount of cold gas, which results from a forming massive gas disc with radius $r > 5$ kpc in the center. Cold gas is trapped on circular orbits and cannot be accreted by the SMBH to fuel the feedback cycle. Li & Bryan (2014) observe a similar disc in their hydrodynamical simulations.

After time $t > 500$ Myr, the jet power hovers between $10^{44} \text{ erg s}^{-1} < L_{\text{jet}} < 10^{46} \text{ erg s}^{-1}$, in agreement with obser-

vational power estimates that are required to inflate X-ray cavities in a sample of CC clusters (e.g., Rafferty et al. 2006). While jets in **Bondi** and **Dense** remain active throughout the simulation time, **Fiducial** and **HD** show more intermittent jet behavior. The jet luminosities in the **Dense** model are on average twice as high as in the **Fiducial** model. In the **Fiducial** model, the low density jets are easily deflected by cold central clumps, yielding drastically varying jet directions. The jets with a much higher momentum density in the **Dense** model, however, keep their direction. Final SMBH masses reach $M_{\text{bh}} \sim 7 - 9 \times 10^9 M_{\odot}$. Consequently, SMBHs grow at most by a factor of 3 over 2 Gyr in line with expectations.

Figure 7 shows the time evolution of the total kinetic energy and mass-weighted average velocity within 200 kpc. The initial velocity fluctuations quickly decay as our non-cosmological set-up does not support continuous driving as a result of gravitational potential fluctuations owing to gas accretion and mergers. Once AGN feedback sets in (at

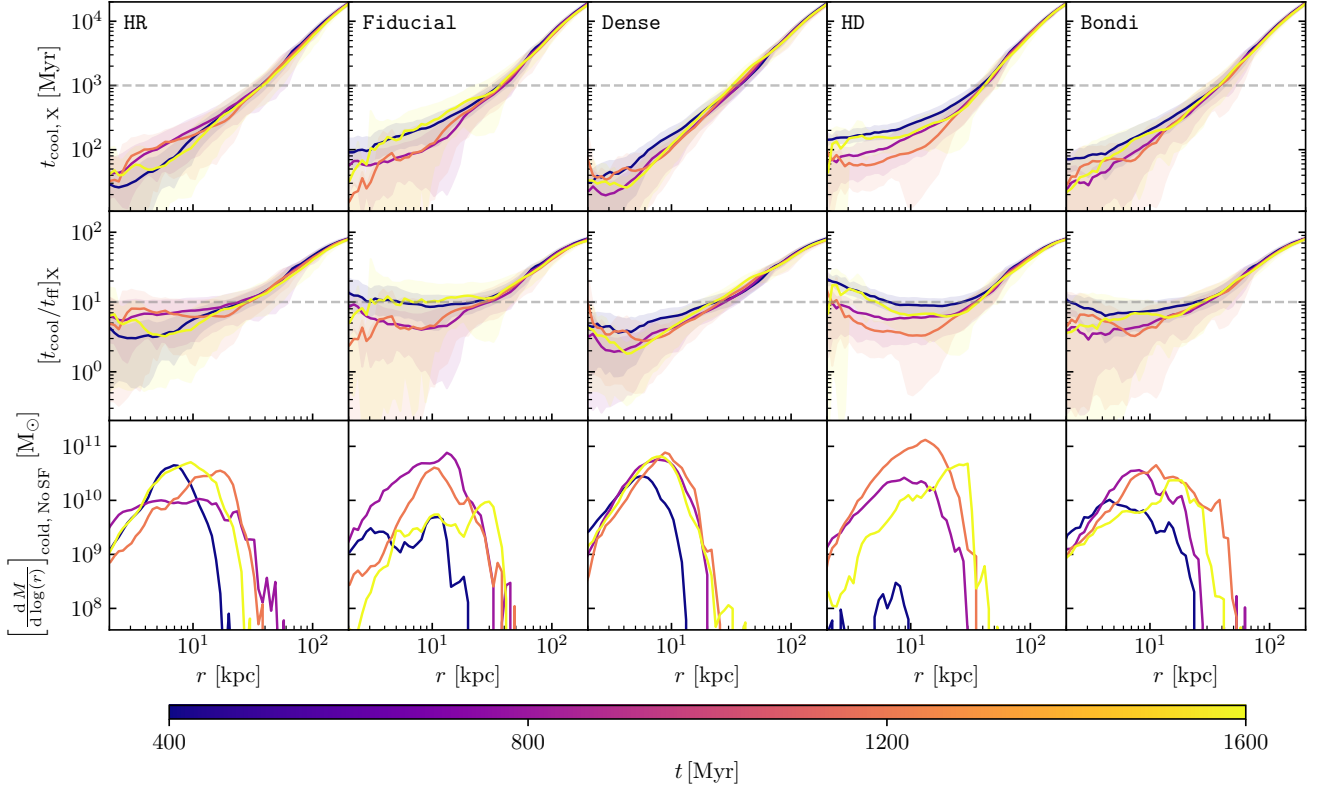


Figure 5. Radial profiles show the X-ray weighted cooling time t_{cool} , the ratio of cooling-to-free fall time $t_{\text{cool}}/t_{\text{ff}}$ and the total mass per bin normalized by the bin size for non-star forming gas with $t_{\text{cool}} < 100$ Myr, i.e., $[dM/d \log(r)]_{\text{cold, No SF}}$. The different colours correspond to simulation times as indicated on the colour bar. Shaded areas indicate the 10th to 90th percentiles. The ratio $t_{\text{cool}}/t_{\text{ff}}$ falls below 10 in the central region ($r \lesssim 50$ kpc), where cold gas forms stars. The minimum in $t_{\text{cool}}/t_{\text{ff}}$ roughly corresponds to the maximum amount of cooling gas mass.

$t > 500$ kpc), kinetic energy is injected into the central regions that self-regulates at a level of $E_{\text{kin}, r < 200 \text{ kpc}} \sim (0.5-1) \times 10^{60}$ erg. This generates mass-weighted average velocities at the level of around $\bar{v}_{r < 200 \text{ kpc}} \approx 75 \text{ km s}^{-1}$, with fluctuations of a factor of two, which are qualitatively similar in our different AGN feedback models (Fiducial, Dense, HD and Bondi). Clearly, simulations without AGN feedback (NoBH and NoBHNoCool) continue to lose kinetic energy. However, radiative cooling leads to a drop in thermal pressure, which initiates motions in the ICM (model NoBH), which partially compensates for the turbulent decay of kinetic energy and thus sustains larger velocities in comparison to our non-radiative model (NoBHNoCool).

In Fig. 8, we show the total mass in star forming gas (top) and non-star-forming gas with $t_{\text{cool}} < 10$ Myr (bottom) while we compare the gas reservoirs in the entire simulation (panels on the left-hand side) and within the accretion radius (panels on the right-hand side). Whereas the amount of star formation and cold gas varies with time, the cluster remains in a state of constant cooling and star formation. However, if the presence of cold gas is intermittent in the accretion region, the SMBH accretion rate reflects this behaviour. Especially in the runs HD and Fiducial, cold gas and star forming gas are temporarily absent in the accretion region.

4 CONNECTING JET ACTIVITY TO OBSERVATIONS OF X-RAY CAVITIES

Jet activity on tens of Myr timescales in CC clusters can be constrained by measuring the energy contained in hot bubbles inflated by AGN driven jets and observed as X-ray cavities. Here, we want to compare the cavity luminosity with the instantaneous jet power and cooling luminosity obtained from the simulations.

4.1 Fitting X-rays cavities in the simulations

To efficiently identify cavities in our simulations with similar constraints as imposed by observations, we first compute the X-ray emissivity I_X within a SMBH-centered image with dimension $150 \text{ kpc} \times 150 \text{ kpc}$ and depth 150 kpc (panels on the left-hand side in Fig. 9). Defining the azimuthally averaged X-ray profile \bar{I}_X , we construct the X-ray fluctuation image via $(I_X - \bar{I}_X)/\bar{I}_X$. To simplify our fitting procedure, we use a coarse grained X-ray image with a bin size of 10 kpc and fit ellipses to contour lines with $\delta I_X/\bar{I}_X = -0.15$. This enables us to compute cavity energies $E_{\text{cav}} = P_{\text{th}}V$, where the thermal pressure P_{th} is the average value at the radius of the bubble center and V is the ellipsoid volume by assuming the depth of the ellipsoid to be equal to the minor axis of the fitted ellipse. We reject any fitted cavities with centers outside a cube of side length of 150 kpc . The cavity luminosity

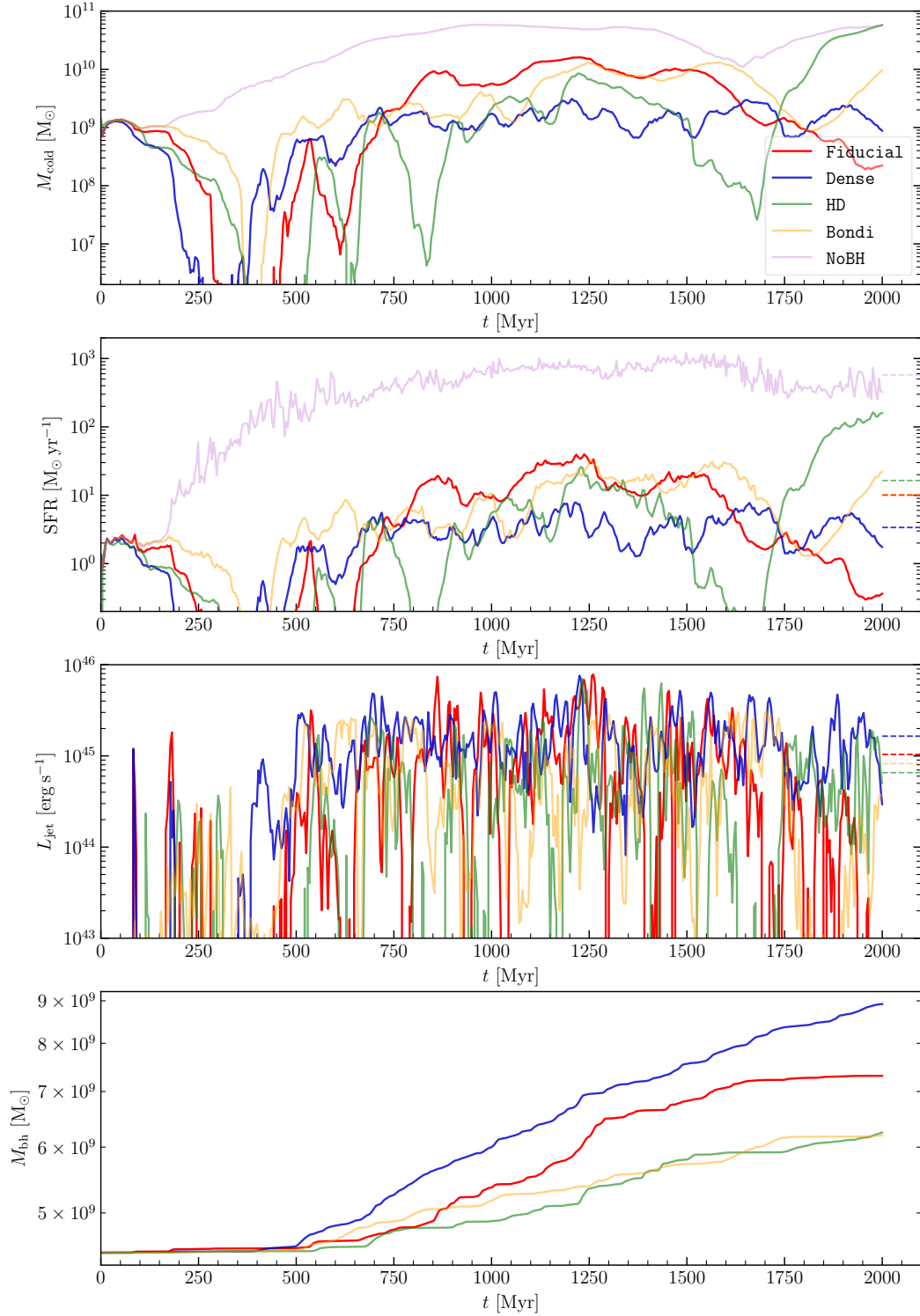


Figure 6. Time evolution of cold gas mass M_{cold} ($T < 10^6$ K), star formation rate SFR, jet power L_{jet} and SMBH mass M_{bh} . Averages for times $t > 500$ Myr are shown with dashed horizontal lines on the right. If no feedback is included (NoBH) runaway cooling is observed and unobserved star formation rates of $> 100 M_{\odot} \text{ yr}^{-1}$. After 500 Myr all feedback models establish a self-regulated state with moderate star formation rates ($\sim 10 M_{\odot} \text{ yr}^{-1}$) and jet powers ($\sim 8 \times 10^{44}$ erg s). Dense jets have a larger momentum density and deposit their energy at larger radii so that the central gas cools more strongly and gives rise to larger SMBH masses in comparison to the other models. The hydrodynamical model forms an unobserved type of massive disc at 2 Gyr with extreme star formation rates ($\sim 100 M_{\odot} \text{ yr}^{-1}$). In Fig. 10 we show histograms of the jet power.

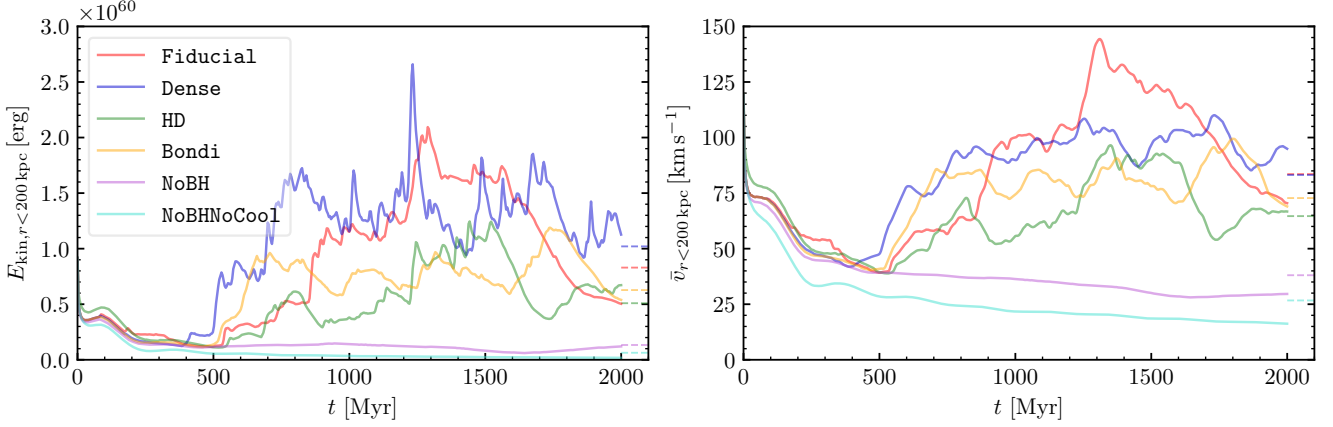


Figure 7. Time evolution of the total kinetic energy within 200 kpc ($E_{\text{kin}, r < 200 \text{ kpc}}$) and mass-weighted average velocity within 200 kpc ($\bar{v}_{r < 200 \text{ kpc}}$). Averages for all times are shown with a dashed horizontal lines on the right. Turbulent velocities that are present in the initial conditions decay as a function of time. The onset of jet feedback at $t > 500$ kpc in runs *Fiducial*, *Dense*, *HD* and *Bondi* injects substantial kinetic energy. On the other hand, runs excluding AGN feedback *NoBH* and *NoBHNoCool* (with and without radiative cooling, respectively) continue to lose kinetic energy.

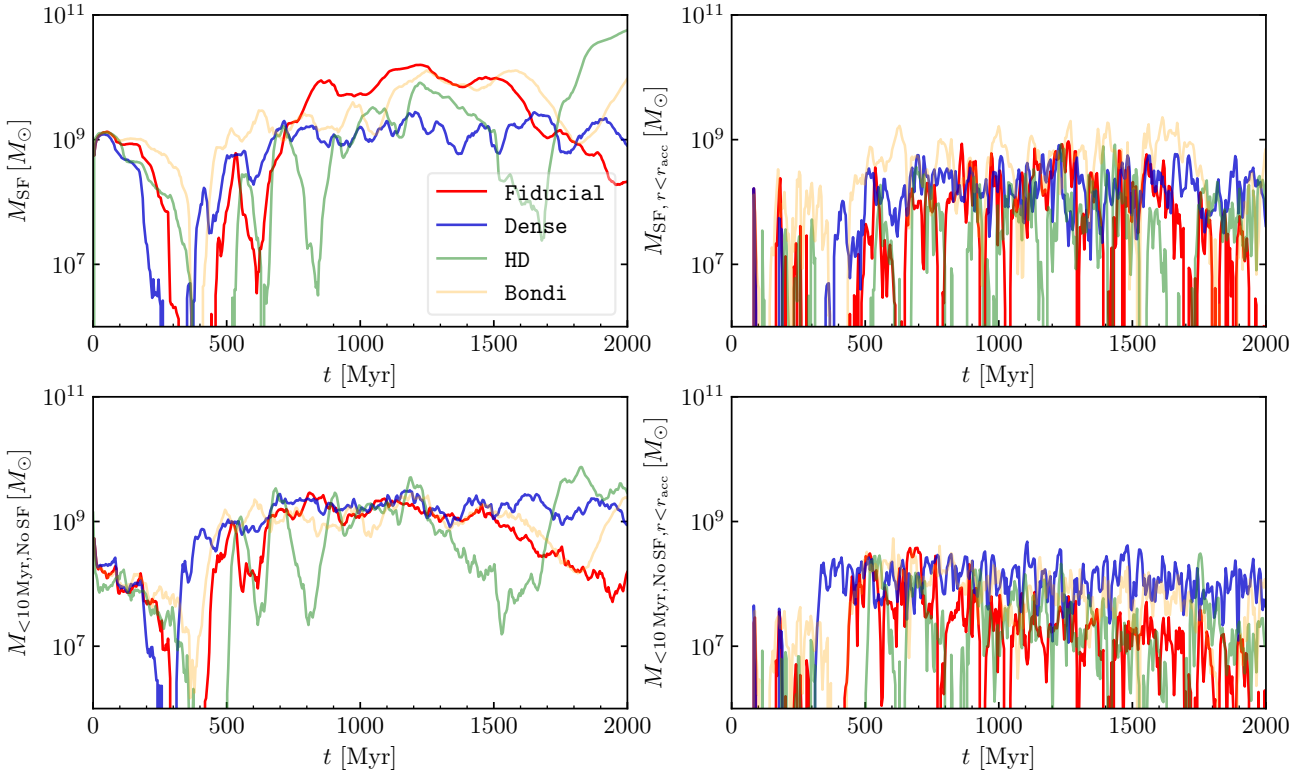


Figure 8. Mass in star forming gas (top) and gas with $t_{\text{cool}} < 10$ Myr (bottom) within the entire simulation (left) and inside the accretion radius, $r < r_{\text{acc}}$ (right). While cold and star forming gas is present throughout the simulation, its presence in the central accretion region is intermittent and varies with time. The gas is dragged up by the AGN and accelerated away from the center.

L_{cav} is then given by

$$L_{\text{cav}} = \frac{E_{\text{cav}}}{t_{\text{rise}}} = \frac{P_{\text{th}}V}{t_{\text{rise}}}, \quad (9)$$

where t_{rise} is the bubble rise time, which we assume to be equal to the sound crossing time t_{sc} ;

$$t_{\text{rise}} = t_{\text{sc}} = R \sqrt{\frac{\mu m_{\text{p}}}{\gamma_{\text{a}} k_{\text{B}} T}} \approx 40 \text{ Myr} \left(\frac{R}{40 \text{ kpc}} \right) \left(\frac{k_{\text{B}} T}{3 \text{ keV}} \right)^{-1/2}, \quad (10)$$

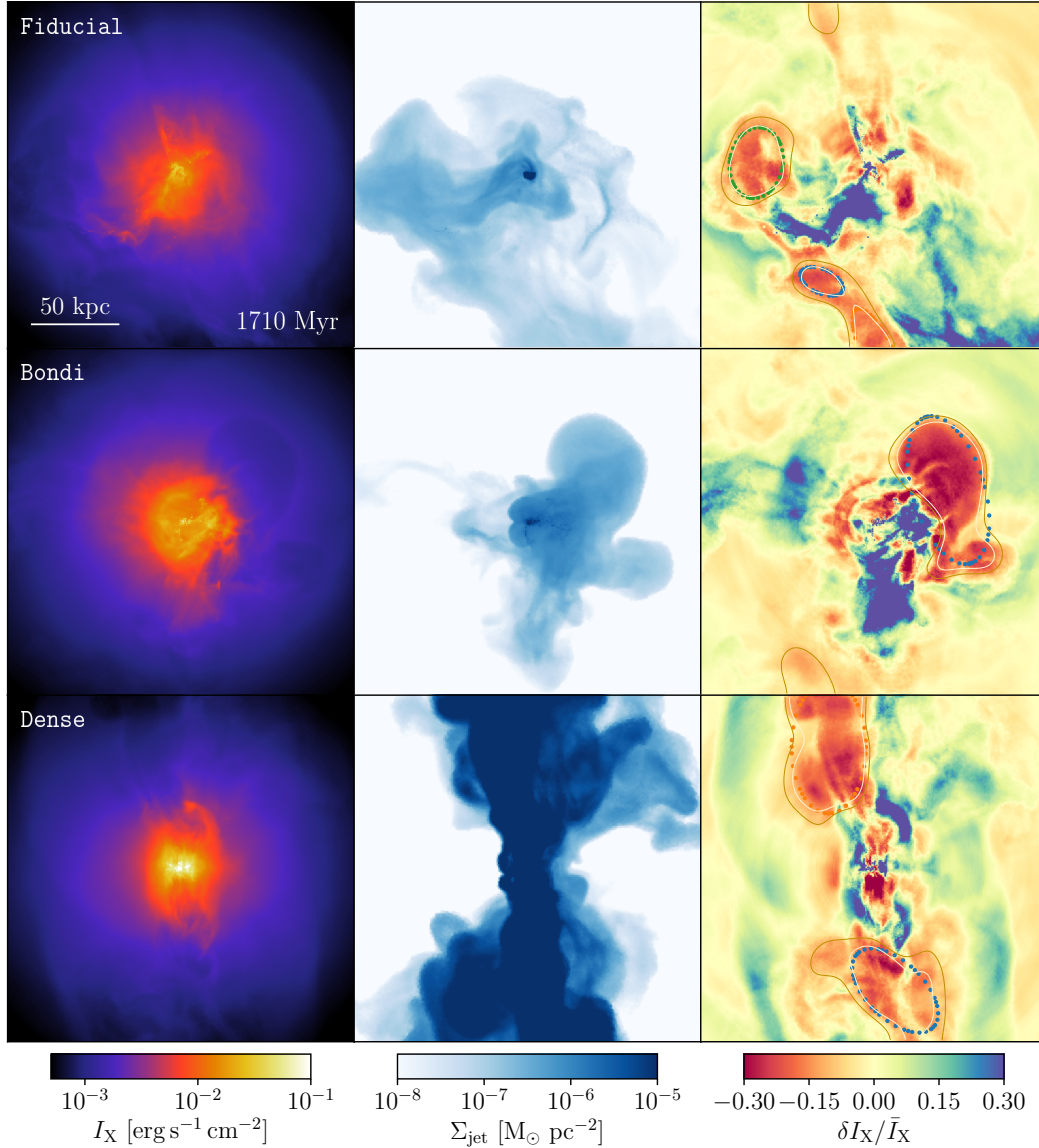


Figure 9. X-ray emissivity in the Chandra band (left column), integrated jet mass surface density (central column), and $\delta I_X/\bar{I}_X$ (right column), at a resolution of 512 pixels \times 512 pixels). The projections maps have been integrated through the entire simulation box, the size of the images are 200 kpc, and we show a simulation time of 1560 Myr. We devise an automated algorithm for finding cavities in the X-ray images by (i) subtracting an azimuthally symmetric profile I_s of the X-ray emissivity and normalizing it with the mean profile, $\delta I_X/\bar{I}_X$, and (ii) fitting ellipses to cavities with a contrast of 15 per cent in the residual maps. Images used for this methods have a resolution of 100 pixels \times 100 pixels and a shallower depth (see Section. 4.1 for details). Cavities in the resulting image at 10 per cent (red) and 15 per cent (gray) are marked with contours and the fitted ellipses are shown with dots. The ellipse volume (where depth is assumed equal to the minor axis) and average pressure at its center are used to determine the cavity power L_{cav} (see Fig. 10).

where $\gamma_a = 5/3$ for the ambient ICM.

The method is able to recover the most relevant cavities. Bubbles can disrupt into smaller cavities during their late-time evolution as a result of Kelvin-Helmholtz instabilities, which are suppressed by magnetic draping (Dursi 2007; Dursi & Pfrommer 2008; Ehlert et al. 2018). An example of such a splitting of an AGN lobe into two smaller bubbles can be observed in the bottom-left corner of the top panel of Fig. 9. Note that our algorithm with the detection threshold is tuned to bubbles inflated by our low-density (fiducial) jets. Therefore, denser bubbles inflated in our model **Dense**

may therefore not be fully recovered, especially if they are small.

In the panels on the right-hand side in Fig. 9, we show $\delta I_X/\bar{I}_X$ at a resolution of 512 pixels \times 512 pixels, projected through the entire simulation box. Low density regions and regions dominated by kinetic energy like the bubbles become discernible as a dip in relative intensity (red). These regions are well captured by our cavity finder. On the other hand, thermally compressed regions and shocks are visible as an increase in relative intensity (blue). Here, regions below the cavities show a strong excess in X-ray emissivity in the upper and central panels, while the lower panel shows bubbles in

the process of being inflated, with signatures of shocks at the bubble-ICM interface. Those are currently not found with our cavity finder.

4.2 Comparing cavity powers to jet powers and cooling luminosities

Figure 10 shows from left to right probability distribution functions (PDFs) of jet power, cavity powers and ICM cooling luminosities within the central 30 kpc for models indicated in the legends. Jet powers encompass a range between 10^{43} – 10^{46} erg s $^{-1}$, where the exact distribution is somewhat model dependent. The jet powers of model **Dense** show a lower scatter with an increased median (dashed lines) compared to the **Fiducial** model, which in turn shows a slightly higher median value than the models **HD** and **Bondi**. Interestingly, median cavity powers are much more similar at ~ 6 – 7×10^{44} erg s $^{-1}$ for all models. ICM luminosities also show a smaller scatter around median values of ~ 7 – 10×10^{44} erg s $^{-1}$.

The main reason that these highly variable jet powers do not result in similar variances of the cavity powers is the high-frequency time variability of these powers. Because cavities are inflated over timescales of ~ 10 s Myr, the cavity powers correspond to average values over at least these timescales. Our algorithm is able to detect old cavities (with a start of the inflation > 100 Myr) out to scales of > 50 kpc, rising in the atmosphere. The continuous inflation of new bubbles with only short times of quiescence of ~ 50 Myr (cf. the evolution of L_{jet} in Fig. 6) causes bubbles to always exist in the cluster and to encompass a combined jet cavity power (L_{cav}) that reaches similar values in our different models. In Fig. 11, we show jet power vs. cavity power on the right, which echoes these results. Jets with $L_{\text{jet}} \lesssim 10^{44}$ erg s $^{-1}$ do not result in separate cavities but instead are contributing to inflating larger, higher luminous cavities. Note that our simulated cavity powers reflect observational estimates of cavity luminosities (Birzan et al. 2004; Rafferty et al. 2006; Diehl et al. 2008).

While the jet power evolutions in Figs. 6 and A1 show periods of jet inactivity in some models, we find that cavities are always present throughout the runtime. This is consistent with observations of 55 cluster of which 60–100 per cent show cavities (Birzan et al. 2012). Interestingly, we find that the jet powers L_{jet} exceed the central cooling luminosities L_{ICM} at most by an order of magnitude. However, jet powers that are up to 2 orders of magnitude lower than cooling luminosities are relatively common. Consequently, AGN feedback keeps the cluster in a state of moderate cooling with low but persistent star formation (e.g., Voit & Donahue 2005; Cavagnolo et al. 2009).

5 MAGNETIC COUPLING OF COLD AND HOT GAS

In this section, we study the morphology and kinematics of the cold gas and how magnetic fields influence it. We also address the relevance of magnetic fields in redistributing the AGN feedback energy and how it is related to the hot-phase observables, such as the velocity distribution of the X-ray emitting gas and the Faraday rotation measure.

5.1 Impact of magnetic fields on cold gas morphology and kinematics

The dynamics in the cluster center is dominated by the jet and its interaction with cold gas (especially for low-density jets). Consequently, a clear connection between cold gas and bubbles is expected. To this end, we analyse the cold gas morphology and kinematics by looking at internal alignment of the cold gas angular momentum. In the following we only consider cold cells with $T < 2 \times 10^4$ K or SFR > 0 which constitute the filamentary structures seen in our simulations. We define the angular momentum of those individual cells of cold gas, $\mathbf{l}_{\text{fil},i} = m_i \mathbf{r}_i \times \mathbf{v}_i$ and calculate the total angular momentum of the cold gas via

$$\mathbf{L}_{\text{fil}} = \sum_i m_i \mathbf{r}_i \times \mathbf{v}_i \quad (11)$$

where we measure all velocity and radius vectors with respect to the cluster center and only account for cold cells according to the criterion defined above. This enables us to compute the alignment statistics of individual cold cells with the total angular momentum by computing the vector product of the normalised cell's angular momentum $\hat{\mathbf{l}}_{\text{fil}}$ with the unit total angular momentum $\hat{\mathbf{L}}_{\text{fil}}$, i.e. $|\hat{\mathbf{L}}_{\text{fil}} \cdot \hat{\mathbf{l}}_{\text{fil}}|$. Figure 12 shows projections of this quantity and PDFs where colors in the lower left corner of each image label individual distributions in the respective PDFs. The formation and presence of individual filamentary structures are transient phenomena on timescales of a 100s of Myr so that sufficient time-sampling is required. PDFs of a single model for different times are compared in the bottom panels, while different models at individual times are shown on the right. Distributions that peak at low values of $|\hat{\mathbf{L}}_{\text{fil}} \cdot \hat{\mathbf{l}}_{\text{fil}}|$ are more random/filamentary than distributions peaking at higher values which are more discy.

In general, the models **Fiducial** and **Bondi** show very elongated filamentary structures extending out to $r \sim 30$ – 50 kpc. We see a coherent kinematic structure along the filaments with a slowly varying angular momentum distribution. While there are also filamentary cold structures in the **Dense** model, they are confined to smaller radii. Magnetic fields in combination with radiative gas cooling cause the formation of these filamentary structures while purely hydrodynamic simulations shatter cooling clouds into small cloudlets as a result of Kelvin-Helmholtz instabilities (Sparre et al. 2020; Müller et al. 2021), similar to the formation of long filamentary tails of jellyfish galaxies.

In the models **Fiducial** and **Bondi**, which enable extended filamentary structures, we only observe transient disc structures in the cold gas phase, which either foster star formation or get accreted onto the SMBH on short timescales of a few 100s of Myr. Importantly, in these models the disc is not continuously fed with gas of similar angular momentum, which is consistent with observations (Russell et al. 2019). By contrast, there are persistent and long-lived discy cold gas morphologies in the **Dense** and **HD** models. In particular, the **HD** model clearly shows a strong discy distribution of the cold gas phase throughout. In model **Dense**, there is a long-lived coherent discy structure at the cluster center, while at radii $r \gtrsim 10$ kpc we observe a more random distribution of filamentary structures. We see that in the presence of a cold-gas disc, the cold gas is much more confined to the center and less volume filling.

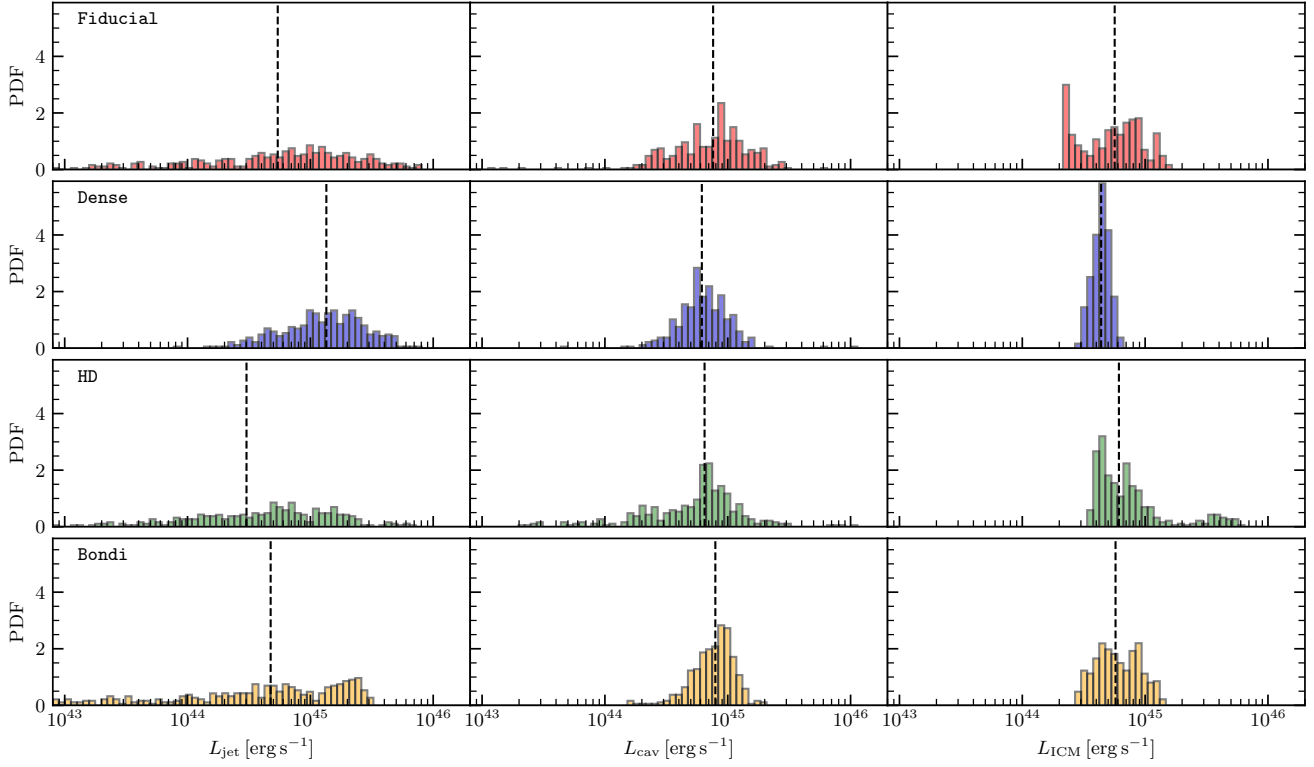


Figure 10. Normalized histograms of the jet power, cavity power, and cooling power within 30 kpc (left to right) of the **Fiducial**, **Dense**, **HD**, and **Bondi** run after 500 Myr. Dashed lines indicate median values. Low-power jet events ($L_{\text{jet}} \lesssim 10^{44} \text{ erg s}^{-1}$) inflate cavities that are systematically missed by our cavity detection algorithm. While the distributions of cooling power and cavity power are very similar, we observe a broader distribution of jet powers with a tail towards low-luminosity events that are triggered by individual cooling filaments.

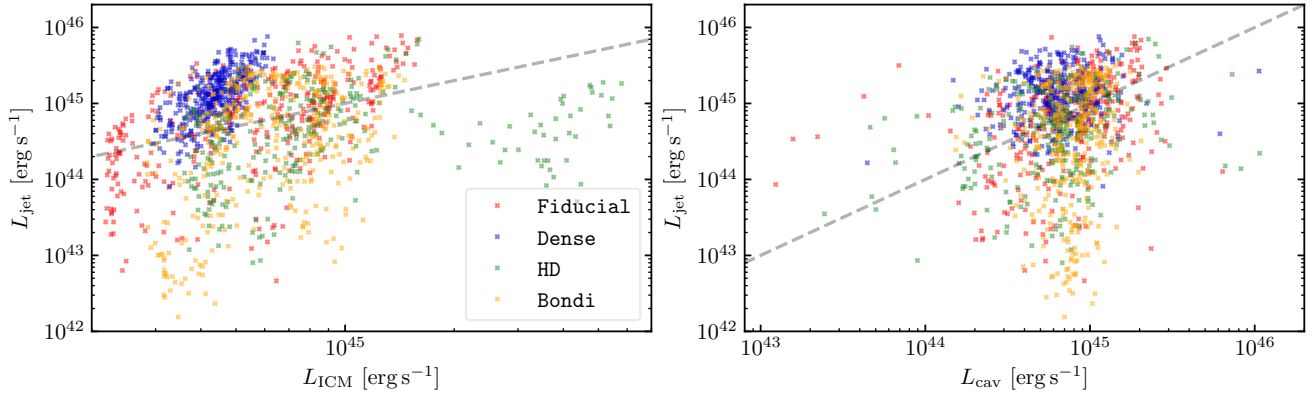


Figure 11. Jet power L_{jet} vs. ICM cooling luminosity L_{ICM} (left) and jet power vs. cavity power (right) after 500 Myr. Jet powers do not necessarily correspond to the current cooling luminosity. Self-regulation is achieved in an average sense on longer timescales. The hydrodynamical run shows an excursion of a phase of stronger cooling, especially at later times when a disc is formed. We note that our cavity powers span two orders in magnitude while the corresponding jet powers span four orders of magnitude.

Magnetic fields allow for a more efficient coupling of cold and hot phases, by efficiently sharing momentum between these two phases through the magnetic pressure and tension forces (Wang et al. 2021). In addition, the increased magnetic field strength in the cooling gas leads to magnetic breaking, reducing angular momentum, which may limit disc formation (Wang et al. 2020). Here, magnetic fields appear to be necessary to transfer jet-induced angular momentum

from the hot phase onto the cooling gaseous phase so that later accreting filaments condense into a central configuration with a different angular momentum distribution, thus precluding the formation of a sustained and massive disc. In general, jets induce turbulence in the central region of the cluster, which interferes with condensing gas. This in combination with the turbulence from the initial conditions affects the dynamics of the cold gas. While we do not follow

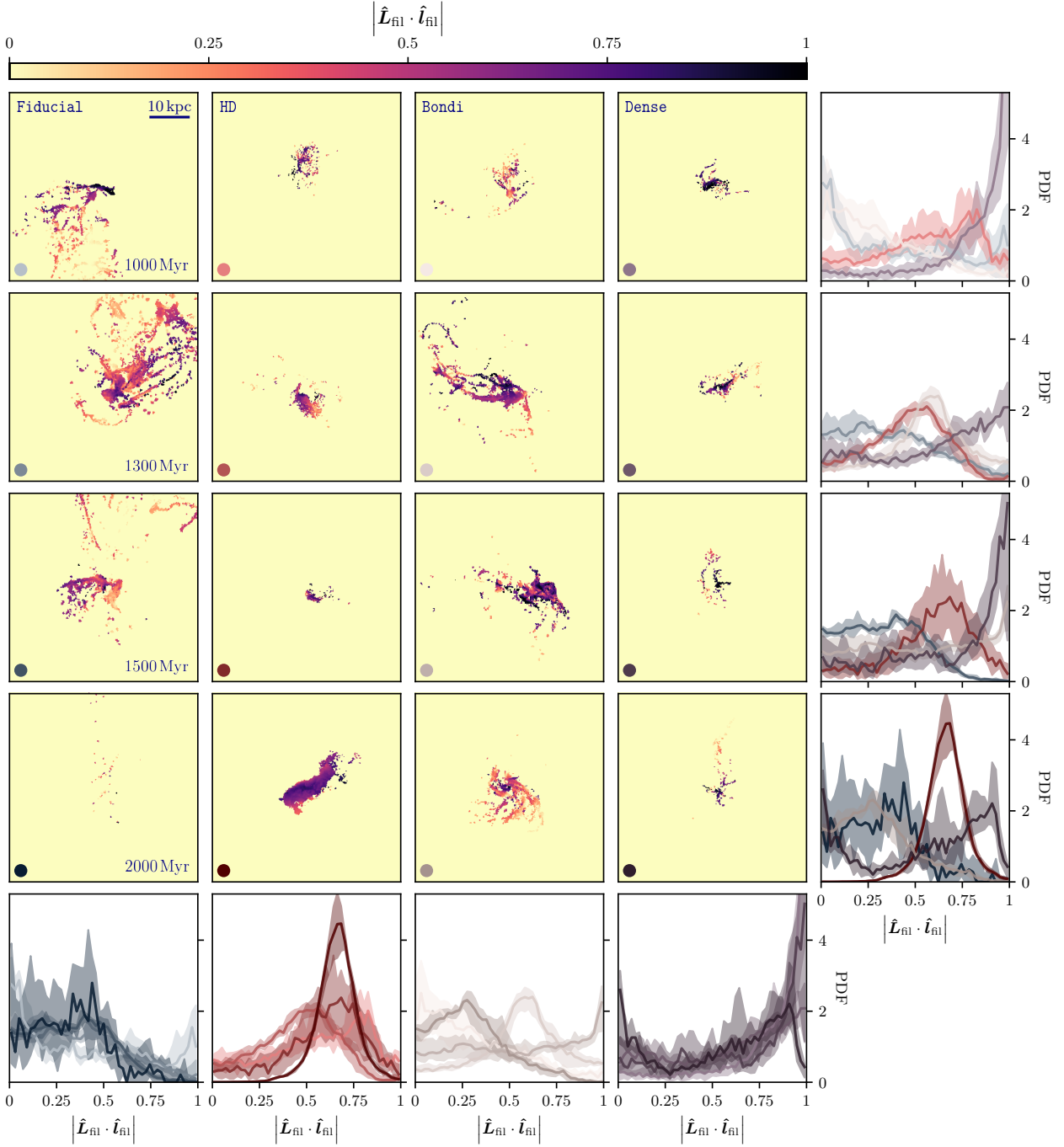


Figure 12. Projection of normalized angle between total angular momentum of the cold gas and that of the individual cells $|\hat{\mathbf{L}}_{\text{fil}} \cdot \hat{\mathbf{l}}_{\text{fil}}|$ at 1000, 1300, 1500 and 2000 Myr (top to bottom) for different runs indicated in the legends (left to right). The bottom (right-most) panels show the PDF of $|\hat{\mathbf{L}}_{\text{fil}} \cdot \hat{\mathbf{l}}_{\text{fil}}|$ of the different panels in the respective columns (rows) with colors in the lower left corners of the panels identifying the corresponding PDFs. A discy distribution implies values of $|\hat{\mathbf{L}}_{\text{fil}} \cdot \hat{\mathbf{l}}_{\text{fil}}| \approx 1$ while a random distribution is flat in this quantity. We see a large variety of gas kinematics over time for the different models while the HD and – to some extent – the Dense models are significantly discier than our MHD models with light jets.

the evolution of the cold gas to the H α and carbon-oxygen (CO) emitting phases, we speculate that the steady injection of momentum in the same direction of the high density jets appears to facilitate the formation of more discy structures that seem to be inconsistent with observed extended filamentary structures surrounding cD galaxies in clusters

(Russell et al. 2019). On the other hand, the deflected low-density jets can lift up cold gas in their wakes and stir the cold gas in more isotropic directions.

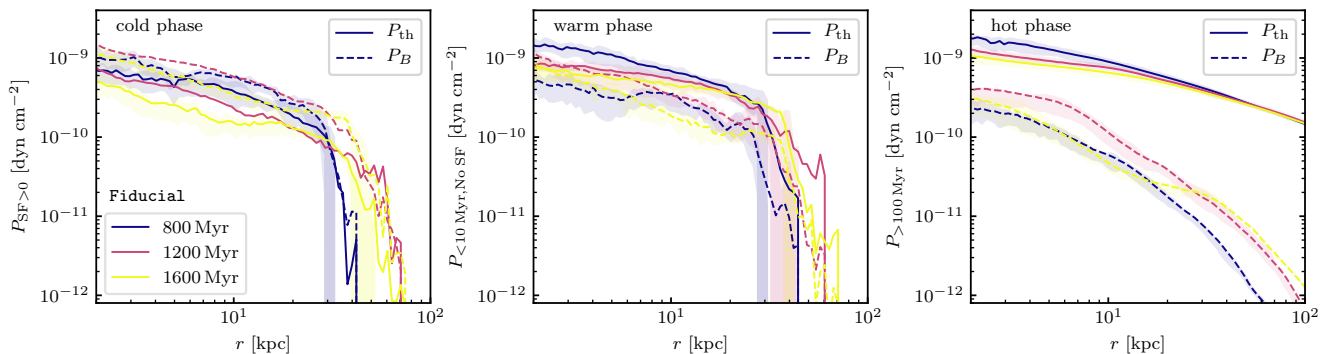


Figure 13. Radial profiles of the thermal pressure (solid) and magnetic pressure (dashed). From left to right, we show the star forming cold gas ($P_{\text{SF}>0}$), non-star forming, warm gas with $t_{\text{cool}} < 10$ Myr ($P_{<10 \text{ Myr, No SF}}$) and hot gas with $t_{\text{cool}} > 100$ Myr ($P_{>100 \text{ Myr}}$). Radial profiles correspond to average profiles within 160 Myr and shaded areas denote the 10th to 90th percentiles. In the cold phase, the magnetic field becomes dynamically relevant because of a loss of thermal support as a result of radiative cooling.

5.2 Influence of the magnetic field on AGN feedback

In Fig. 13, we show radial profiles of the thermal (solid) and magnetic (dashed) pressure in the model *Fiducial* at different times. From left to right, we show profiles in the cold phase ($\text{SFR} > 0$), warm phase ($t_{\text{cool}} < 10$ Myr, $\text{SFR} = 0$) and hot phase ($t_{\text{cool}} > 100$ Myr). Magnetic fields become progressively more dynamically relevant for colder phases to the point where the cold phase is dominated by magnetic pressure (Wang et al. 2021). Consequently, magnetic fields will play a significant role in the dynamics of filaments. Note, as our ISM model prevents cooling to observed temperatures that are orders of magnitudes lower than in our model, we expect thermal pressure losses due to additional cooling to increase the magnetic fields even further. Consequently, the implications for stability and dynamics are expected to be even more severe.

As discussed in Ehlert et al. (2021), magnetic fields and velocity fields are inherently coupled via the induction equation and the equation of motion. It may therefore be instructive to look at the velocity field here. In Fig. 14, we show slices of the absolute velocity $|\mathbf{v}|$, line-of-sight velocity dispersion σ_{los} of the X-ray emitting gas ($k_B T < 15$ keV) with contours of a jet tracers on a cut-plane through the cluster center, slices of the absolute magnetic field $|\mathbf{B}|$, the magnetic-to-thermal pressure ratio X_B , the total pressure P_{tot} , and the Faraday rotation measure:

$$\text{RM} = \frac{e^3}{2\pi m_e^2 c^4} \int_0^L n_e \mathbf{B} \cdot d\mathbf{s}, \quad (12)$$

where the integral extends along the line of sight from the source to the observer, e is the elementary charge and m_e is the electron rest mass. The magnetic field and thermal electron density are results of our simulations. For gas that is not forming stars, we directly use the thermal electron density as calculated in the cooling module of the code. For star-forming gas, we need to account for the subgrid-scale model of the ISM (Springel & Hernquist 2003) used in our simulations. This model implicitly assumes an unresolved multi-phase ISM consisting of a volume-filling warm phase and a neutral cold phase at 10^4 K that dominates the gas mass. Hence, in order to calculate the contribution to

the Faraday rotation measure of star-forming gas, we self-consistently calculate gas that our subgrid model assigns to the volume-filling warm phase as laid out in Springel & Hernquist (2003) and assume that it is fully ionised. Note that we may still overestimate the electron number density as the AGN outflow may contain a molecular gas component that we do not account for here.

In Fig. 14, the high-velocity jet is discernible especially in the *Dense* model, where the jet faces minimal deflection. However, corresponding line-of-sight velocities are small $\sigma_{\text{los}} \sim 120 \text{ km s}^{-1}$. In contrast, the *HR* and *Fiducial* models show multiple pixels with $\sigma_{\text{los}} \gtrsim 180 \text{ km s}^{-1}$ at this time. Here, larger fractions of the velocity are diverted into the line of sight. Due to the persistent jet directions in model *Dense*, the enhancement of the ICM velocity dispersion is limited to a cone region in jet direction. On the other hand, low-density jets induce more isotropic turbulence, which is reflected in the velocity dispersion maps where increased values coincide with the jet location. Propagating jets induce shocks in the ICM that are clearly discernible as regions of increased P_{tot} in Fig. 14. While shocks in runs with low density jets appear spherical, the shocks in simulation *Dense* are more ellipsoidal and therefore mostly interact in the direction perpendicular to the direction of jet injection.

In our simulations, jets amplify the magnetic field in the wake to values of order $100 \mu\text{G}$, as a result of converging gas flows that compress the gas (Ehlert et al. 2021). This increases the cooling rate so that the thermal gas quickly loses pressure support to the point where the magnetic pressure dominates over the thermal pressure, i.e., $X_B \gtrsim 1$. In these regions, the magnetic tension force withstands the turbulent motions in the ICM, giving rise to comparably straight filaments (see Fig. 14). Note that fluctuations in the total pressure appear due to jet-induced shocks. There is no obvious correlation between total pressure and the magnetic field structure, implying that these highly magnetized filaments are in approximate pressure equilibrium with the surrounding ICM.

By construction, our initial magnetic field strength $X_{B,\text{ICM}} = 0.0125$ yields bulk rotation measures that are in agreement with observations (Clarke 2004; Murgia 2011). However, in the regions of strong magnetic field, the rotation

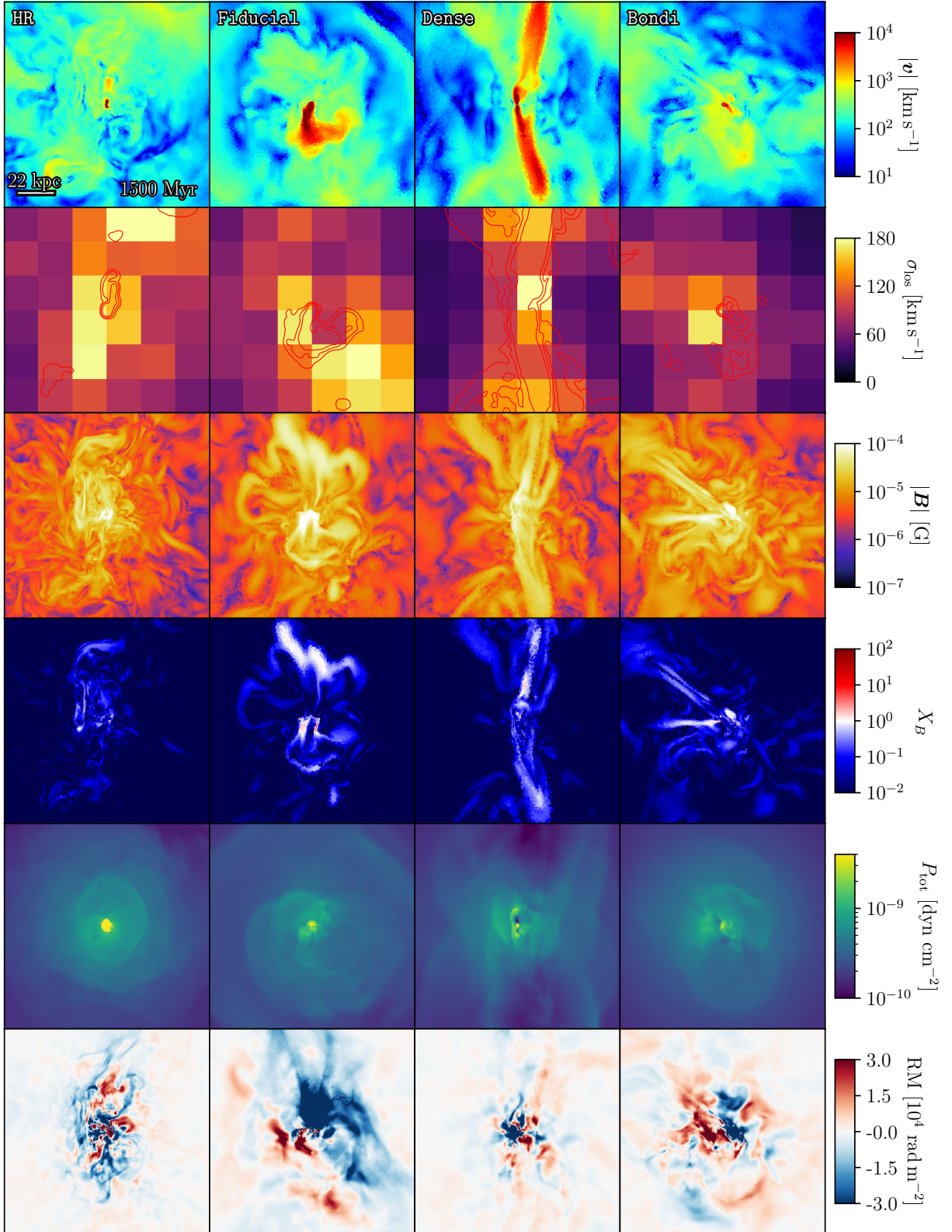


Figure 14. From top to bottom, we show slices of the velocity $|v|$, X-ray weighted mean line-of-sight velocity dispersion, slices of the magnetic field, magnetic-to-thermal pressure ratio X_B , total pressure P_{tot} and Faraday rotation measure at 1500 Myr. Contours correspond to jet tracer values of 10^{-4} , 10^{-3} and 10^{-2} in a midplane slice. Jet induced turbulence is visible as increased velocity dispersion. In our model **Dense**, high momentum-density jets propagate nearly unperturbed and cause conically enhanced velocities and velocity dispersion while low-momentum density jets in the three other models are more easily deflected, which results in more isotropic velocity fields. The magnetic field is strongly amplified in the wake of the jets due to increased cooling rates that are triggered by converging gas flows giving rise to substantial rotation measure values.

measure reaches values in excess of $RM > 3 \times 10^4 \text{ rad m}^{-2}$, which is an order of magnitude above observed values. However, the rotation measure morphology is a strong function of numerical resolution (bottom two panels of Fig. 14). We see alternating regions with differing signs of the Faraday rotation measure on small angular scales, suggesting that beam smoothing effects and other observational uncertainties may bring our simulations closer to the observed results (e.g., Newman et al. 2002; Johnson et al. 2020). Most importantly, the amplified magnetic field stays generally confined to the path of the bubble on simulated timescales. Thereby, low-density jets amplify magnetic field more isotropically compared to the unidirectional jets in our **Dense** model.

6 DISCUSSION

In this paper, we examined simulations of isolated CC galaxy clusters including radiative cooling, star formation and black-hole accretion-regulated feedback from AGN driven jets. We explore variations of different aspects of the simulations including the presence of magnetic fields, the SMBH accretion rate model, the density of the AGN driven jet as well as efficiency parameters. In all our simulations, radiative cooling is on average well-balanced by heating from AGN-driven jets, with at most a factor of a few higher instantaneous jet luminosities (compared to the halo cooling losses), but at times also orders of magnitude lower luminosities (Fig. 11).

6.1 Self-regulated CC clusters

In all explored model variations that include jets, the SFR in the cluster is suppressed by at least one order of magnitude compared to the no-feedback case (Fig. 6), yet the thermodynamic profiles remain characteristic for CC galaxy clusters, i.e. with high central densities at or exceeding 0.3 cm^{-3} , central temperatures below 2.5 keV, and entropies well below 10 keV cm^2 (Fig. 4). A *gentle* mode of AGN feedback has also been demonstrated in simulations by Yang & Reynolds (2016); Li et al. (2017); Meece et al. (2017); Bourne & Sijacki (2021), which they attribute to jet-induced shock heating and mixing. Furthermore, our jet feedback is unable to convert CC to non-CC clusters as also seen by Hahn et al. (2017); Chadayammuri et al. (2021). In line with the resulting CC characteristics, a substantial amount of the central ICM gas remains in a state where cooling times are low compared to the free-fall time (Fig. 5), cold gas is constantly present in the cluster (Fig. 8), yet only a small, highly time-variable fraction of it directly feeds the SMBH in the center, causing the instantaneous jet luminosities to fluctuate substantially (Fig. 10). While the presence of cold gas is universal, we find its properties to be highly dependent on different modeling choices: our fiducial model of a magnetized ICM heated by light jets tends to create transient gas filaments with low circularity parameters (i.e. either on predominantly radial or uncorrelated orbits) extending several tens of kpc from the center, while two model variations create cold gas structures with large circularity parameter, i.e. coherent, disc-like rotation (Fig. 12). This includes the simulation without magnetic fields, indicating that continuous feeding of gas with the same angular momentum is precluded

by magnetic fields interconnecting the hot and cold phases. Even in the presence of magnetic fields, the model employing a dense jet produces coherently rotating cold gas discs, however, significantly more compact ones than the ones in the HD case. A plausible reason for this is the directionality of the jet that clearly constrains the direction of resulting lobe structures (a proxy for the large-scale gas flow patterns) in the case of dense jets, but not in the case of light jets (Fig. 9). This implies that in the case of low-density jets, centrally forming cold gas is dragged around by large-scale turbulent motions in the central region of the cluster, while dense jets facilitate a more coherent flow pattern that facilitates the buildup of a rotating disc. The resulting continuous presence of cold gas near the SMBH for dense jets leads to increased accretion rates as seen in Figure 6.

We fitted ellipses to X-ray images of our simulations to more easily connect our simulations to observations of X-ray cavities. Our cavity luminosities are in the range $10^{44} \text{ erg s}^{-1} \lesssim L_{\text{cav}} \lesssim 3 \times 10^{45} \text{ erg s}^{-1}$ across simulations, which is in general agreement with the observed total bubble luminosity in Perseus (Birzan et al. 2004; Rafferty et al. 2006; Diehl et al. 2008). The corresponding spread in cavity luminosities of four orders of magnitude agrees with the variance observed when looking at cluster samples at similar ICM luminosities (see Fig. 6 in Rafferty et al. 2006).

We found a successful solution for self-regulation in a Perseus-like cluster based on physical principles. However, the shallower potential of groups and smaller clusters is expected to show a different coupling efficiency of the AGN and the ICM as suggested by Prasad et al. (2020). On the other hand, in the Phoenix cluster, one of the most massive clusters observed, AGN feedback appears to be too inefficient to halt cooling (McDonald et al. 2019). Therefore more simulations across the cluster mass range in a cosmological setting are required to demonstrate that the presented models are able to successfully self-regulate CC clusters. Nevertheless, our work opens up an avenue to simulate realistic CC clusters in cosmological zoom-in simulations and to finally answer the question about the origin of the bimodality of CC and non-CC systems.

6.2 Accretion models and jet propagation direction

For our simulated scales the exact accretion model has limited relevance. Both Bondi and chaotic cold accretion are very sensitive to dense, cold gas, which makes up the majority of gas accreted in our runs (see Fig. 8). The additional continuous accretion in the Bondi model leads to small outbursts with limited influence on the cluster. In agreement with simulations by Meece et al. (2017), we find that the exact triggering mechanism is secondary for runs with sufficiently high resolution. For the cold accretion model, CCs stay intact independent of probed choices for ϵ and η . However, our run with $\epsilon = 1$, $\eta = 0.0001$ grows the SMBH to $M > 10^{11} M_{\odot}$ within 2 Gyr (see Fig. A1), while observed most massive SMBHs have smaller masses: $6.6 \times 10^{10} M_{\odot}$ (TON 618; Shemmer et al. 2004), $5.1 \times 10^{10} M_{\odot}$ (MS0735-BCG; Dullo 2019), $4 \times 10^{10} M_{\odot}$ (Holmberg 15A; Mehrigan et al. 2019). Observational biases should favor more massive SMBHs rather than smaller ones. In addition, King (2016) shows that active SMBHs can grow to a maximum mass $M_{\text{max}} \simeq 5 \times 10^{10} M_{\odot}$ for typical parameters and only reach

$2 \times 10^{11} M_{\odot}$ in rather extreme cases over a Hubble time. Hence, we conclude that this parameter combination is unlikely to be realised in nature.

We parametrise our accretion models by two variables, the accretion efficiency ϵ in the cold accretion model and the accretion-to-jet power conversion efficiency, η . We find that the total jet efficiency, i.e. the product of the two, $\epsilon\eta$ is most important for describing the properties of the ICM rather than varying both parameters individually (see Fig. A1 and Appendix A for the detailed analysis). In particular, we find that the jet efficiency $\epsilon\eta$ determines the level of intermittency in our runs. More efficient jets (higher $\epsilon\eta$) are able to temporarily push and/or drag cold gas out from the central regions. Lower efficiencies force the jet to be active at all times, limiting jet powers to the maximum while extra cooling is converted into star formation. On the other hand, more energetic outbursts from high-power jets can increase cooling times on larger scales, which can possibly reduce the amount of newly collapsing gas and stabilize the atmosphere more efficiently. However, we note that generally cooling gas with $t_{\text{cool}} < 10$ Myr and star formation are always present in all simulations. The large variety of efficiency parameters (with $\eta = 1$) of self-regulated feedback models used by other research groups generally confirm our findings, which range from $\epsilon = 6 \times 10^{-5}$ (Prasad et al. 2015), $\epsilon = 10^{-4}$ (Prasad et al. 2020), $\epsilon = 5 \times 10^{-4}$ (Prasad et al. 2018), $\epsilon = 10^{-3}$ (Li & Bryan 2014; Meece et al. 2017), $\epsilon = 5 \times 10^{-3}$ (Wang et al. 2019) to $\epsilon = 10^{-2}$ (Li et al. 2015). While these models vary in exact jet powers and SFRs, we consider the similarities of the self-regulated state reassuring considering the vast spectrum of codes, jet models, ISM implementations and resolutions used. More detailed analysis is required to constrain specific parameters.

Our clusters are in a state of condensation with minimum cooling-to-free fall time ratios $\min(t_{\text{cool}}/t_{\text{ff}}) < 10$, with some a fraction of the ICM reaching $\min(t_{\text{cool}}/t_{\text{ff}}) < 1$ (see Fig. 5 middle panel). Previous simulations generally report instability for gas with $t_{\text{cool}}/t_{\text{ff}} < 10$ (Sharma et al. 2012; Gaspari et al. 2012, 2015; Choudhury et al. 2019). Observations of cold filaments in clusters find similar values (Voit & Donahue 2015) but also somewhat larger values in the range $10 \lesssim t_{\text{cool}}/t_{\text{ff}} \lesssim 25$ (Pulido et al. 2018; Olivares et al. 2019). The low end of the entropy distribution at a certain radius may explain high values in clearly thermally unstable clusters (Voit 2021).

As discussed in Section 2.3, the random nature of (chaotic cold) accretion limits the expected jet precession considerably. However, we find that the exact jet direction is extremely important for heavy jets because their high-momentum density implies a fast transport to larger radii and minimizes the lateral heating rate so that the gas quickly becomes thermally unstable and feeds the SMBH perpendicular to the jet direction. Varying the jet direction should have a smaller impact on the self-regulation in the light-jet models because their propagation direction is determined by deflection events off of cold gas filaments and clouds, leading to more isotropic heating in the central regions owing to the increased lateral momentum deposition.

6.3 H α and CO filaments and the role of non-thermal components

While observed filaments reach down to smaller temperatures than simulated here, we argue that comparing our results to observations is nevertheless instructive. Observed filaments in H α and CO show a large distribution of morphologies, ranging from disc-dominated to filamentary structures that can extend over several kpc in length (e.g., Russell et al. 2016; Gendron-Marsolais et al. 2018). Most cold gas and filaments are located below or near bubbles (see Fig. 3). In addition, smooth velocity gradients along the filaments support the idea that buoyantly rising bubbles lift central cold gas and/or lifted gas becomes thermally unstable and cools (Russell et al. 2019). This agrees with our results on the kinematics and morphology of cold phase filaments (see Fig. 12). Beckmann et al. (2019) analyse cold gas in their hydrodynamical simulations and find that filaments are easily shattered by the jet leading to overly clumpy morphologies compared to observations. While we defer a detailed analysis to future work, we also notice clumps in our simulations that are not directly connected in filaments.

In general, the exact details of the feedback loop sensitively depend on the cooling processes via the thermal instability which is in turn sensitive to resolution effects (Martizzi et al. 2019), limiting the scope of detailed quantitative predictions from our simulations. However, our higher resolution runs confirm the findings discussed throughout the paper (see Appendix B for details). In addition, a detailed analysis of resolution dependencies for the jet can be found in Weinberger et al., in prep.

Magnetic fields lead to a strong coupling between cold and hot gas phases (Wang et al. 2021), by sharing momentum between these two phases through the magnetic pressure and tension forces. As a result, the cold phase adopts a more filamentary morphology (Sparre et al. 2020) as magnetic draping suppresses Kelvin-Helmholtz instabilities (Ruszkowski et al. 2007; Dursi 2007; Dursi & Pfrommer 2008; Ehlert et al. 2018). As such, magnetic fields preclude the formation of long-lived cold discs in the first place and do not have to disrupt an already formed disc. In addition, magnetic fields provide substantial pressure support to the cold gas.

Analogously, cosmic ray protons prone to the streaming instability can potentially provide stability to H α filaments and provide heating to power the emission (Ruszkowski et al. 2018). In addition, Alfvén heating from streaming cosmic ray protons may be the dominant heating mechanism in CC clusters with profound implications on the dynamics of the cluster and the resulting feedback cycle (e.g., Guo & Oh 2008; Pfrommer 2013; Jacob & Pfrommer 2017; Ruszkowski et al. 2017; Ehlert et al. 2018; Wang et al. 2020). We defer their inclusion to future work.

7 CONCLUSIONS

Jet feedback is able to stabilize CC galaxy clusters against thermal collapse. We employ MHD simulations to study AGN feedback in an idealised turbulent Perseus-like cluster. Our findings can be summarized as follows:

- Independent of the accretion model (Bondi vs. chaotic

cold accretion), probed accretion efficiency, magnetisation of the cluster and jet density, the cluster settles into a state of self-regulation after ~ 500 Myr (see Figs. 6 and A1) with density, entropy and cooling time consistent with observed CC clusters (see Fig. 4).

- More efficient jet feedback leads to more intermittent jet power and star formation (see Figs. 6 and A1).

- Our fiducial low-density jets are easily deflected by cold gas, which leads to more isotropic turbulence injection and bubble distributions (see Fig. 3). The dense jets form bubble distributions almost exclusively in the jet direction (see Fig. 9). Here, cooling gas is continuously funneled onto the SMBH perpendicular to the jet direction, which leads to quick accretion from a discy distribution that is much more confined to the cluster center ($r \lesssim 10$ Myr, see Fig. 12).

- Our purely hydrodynamic run forms a massive disc ($r \gtrsim 10$ kpc) for $t \gtrsim 200$ Myr (see Fig. 12) which leads to unrealistically high SFRs (see Fig. 6). Transient disc formation that is not long-lived in our MHD runs supports the idea that magnetic fields anchored in the hot phase redistribute angular momentum with the cooling gaseous phase so that filaments accreting later settle into a central configuration with a different angular momentum distribution, thus precluding the formation of a sustained and massive disc.

- In broad agreement with observations, a plethora of cold gas morphologies ranging from discy to very extended filamentary structures is observed across our MHD runs but morphology and extent ($r < 40$ kpc) varies significantly with time in individual runs (see Fig. 12).

- Our inferred luminosities from cavity size measurements correspond to averaged jet powers that are therefore insensitive to periods of short and low-luminosity jet injection. Our imposed temperature threshold for cold accretion leads to ~ 50 Myr long breaks in jet injection in comparison to the continuous accretion condition prescribed in the Bondi model. However, the long life-time of cavities of > 100 Myr since injection leads to a comparable presence of cavities for both models (see Fig. 11).

- The magnetic field is strongly amplified in the wake of the jets due to the increased cooling rates that are triggered by converging gas flows, giving rise to substantial rotation measure values (see Fig. 14).

AGN feedback has been established as the main heating source that allows CCs to reach a state of self-regulation at the observed levels. In order to rule out any specific accretion and jet models, secondary observables such as bubble and cold gas morphologies are needed.

In a next step, accounting for the cosmological assembly of a galaxy cluster is crucial for obtaining a more realistic environment and evolution. We find that light AGN jets are required to obtain the observed extended filaments with an averaged isotropic distribution of the kinematics of filaments. Numerically converged heating rates in the light-jet model imply a minimum resolution of 0.6 kpc in the jet launching region (Weinberger et al., in prep.). We caution that further zooming into the accretion region could reveal distinct small-scale differences for the accretion model (Bondi vs. chaotic cold accretion). In addition, future work will model the cold gas more accurately so that we may disentangle different AGN models by means of the observed distributions of H α and CO filaments.

ACKNOWLEDGEMENTS

KE and CP acknowledge support by the European Research Council under ERC-CoG grant CRAGSMAN-646955 and ERC-AdG grant PICO GAL-101019746. This work was supported by the Natural Sciences and Engineering Research Council of Canada (NSERC), funding reference #CITA 490888-16. The authors gratefully acknowledge the Gauss Centre for Supercomputing e.V. (www.gauss-centre.eu) for funding this project by providing computing time on the GCS Supercomputer SuperMUC-NG at Leibniz Supercomputing Centre (www.lrz.de).

DATA AVAILABILITY

The data underlying this article will be shared on reasonable request to the corresponding author.

REFERENCES

- Abdulla Z., et al., 2019, *Astrophys. J.*, 871, 195
 Beckmann R. S., Dubois Y., 2022, preprint(arXiv:2204.03629)
 Beckmann R. S., et al., 2019, *Astron. Astrophys.*, 631, A60
 Bîrzan L., Rafferty D. A., McNamara B. R., Wise M. W., Nulsen P. E. J., 2004, *Astrophys. J.*, 607, 800
 Bîrzan L., Rafferty D. A., Nulsen P. E. J. J., McNamara B. R., Röttgering H. J. A. A., Wise M. W., Mittal R., 2012, *Mon. Not. R. Astron. Soc.*, 427, 3468
 Blandford R. D., Znajek R. L., 1977, *Mon. Not. R. astr. Soc.*, 179, 433
 Blanton E. L., Sarazin C. L., McNamara B. R., 2003, *Astrophys. J.*, 585, 227
 Bondi H., 1952, *Mon. Not. R. Astron. Soc.*, 112, 195
 Bourne M. A., Sijacki D., 2017, *Mon. Not. R. Astron. Soc.*, 472, 4707
 Bourne M. A., Sijacki D., 2021, *Mon. Not. R. Astron. Soc.*, 506, 488
 Bourne M. A., Sijacki D., Puchwein E., 2019, *Mon. Not. R. Astron. Soc.*, 490, 343
 Cavagnolo K. W., Donahue M., Voit G. M., Sun M., 2008, *Astrophys. J.*, 683, L107
 Cavagnolo K. W., Donahue M., Voit G. M., Sun M., 2009, *Astrophys. J. Suppl. Ser.*, 182, 12
 Cavagnolo K. W., McNamara B. R., Wise M. W., Nulsen P. E., Brüggner M., Gitti M., Rafferty D. A., 2011, *Astrophys. J.*, 732, 71
 Chadayammuri U., Tremmel M., Nagai D., Babul A., Quinn T., 2021, *Mon. Not. R. Astron. Soc.*, 504, 3922
 Chen Y.-H. H., Heinz S., Enßlin T. A., 2019, *Mon. Not. R. Astron. Soc.*, 11, 1939
 Choudhury P. P., Sharma P., Quataert E., 2019, *Mon. Not. R. Astron. Soc.*, 488, 3195
 Churazov E., Forman W., Jones C., Böhringer H., 2003, *Astrophys. J.*, 590, 225
 Clarke T. E., 2004, *J. Korean Astron. Soc.*, 337, 337
 Croston J. H., Hardcastle M. J., 2014, *Mon. Not. R. Astron. Soc.*, 438, 3310
 Croston J. H., Ineson J., Hardcastle M. J., 2018, *Mon. Not. R. Astron. Soc.*, 476, 1614
 Diehl S., Li H., Fryer C. L., Rafferty D., 2008, *Astrophys. J.*, 687, 173
 Dullo B. T., 2019, *Astrophys. J.*, 886, 80
 Dursi L. J., 2007, *Astrophys. J.*, 670, 221
 Dursi L. J., Pfrommer C., 2008, *Astrophys. J.*, 677, 993

- Ehlert K., Weinberger R., Pfrommer C., Pakmor R., Springel V., 2018, *Mon. Not. R. Astron. Soc.*, 481, 2878
- Ehlert K., Pfrommer C., Weinberger R., Pakmor R., Springel V., 2019, *Astrophys. J. Lett.*, 872, L8
- Ehlert K., Weinberger R., Pfrommer C., Springel V., 2021, *Mon. Not. R. Astron. Soc.*, 503, 1327
- Fabian A. C., 2012, *Annu. Rev. Astron. Astrophys.*, 50, 455
- Fogarty K., Postman M., Connor T., Donahue M., Moustakas J., 2015, *Astrophys. J.*, 813, 117
- Fujita Y., Kawakatu N., Shlosman I., Ito H., 2016, *Mon. Not. R. Astron. Soc.*, 455, 2289
- Gaspari M., Ruszkowski M., Sharma P., 2012, *Astrophys. J.*, 746, 94
- Gaspari M., Brighenti F., Temi P., 2015, *Astron. Astrophys.*, 579, A62
- Gaspari M., Temi P., Brighenti F., 2017, *Mon. Not. R. Astron. Soc.*, 466, 677
- Gendron-Marsolais M., et al., 2018, *Mon. Not. R. Astron. Soc.*, 479, L28
- Guo F., Oh S. P., 2008, *Mon. Not. R. Astron. Soc.*, 384, 251
- Hahn O., Martizzi D., Wu H. Y., Evrard A. E., Teyssier R., Wechsler R. H., 2017, *Mon. Not. R. Astron. Soc.*, 470, 166
- Heinz S., Brüggem M., Young A., Levesque E., 2006, *Mon. Not. R. Astron. Soc. Lett.*, 373, 65
- Hillel S., Soker N., 2014, *Mon. Not. R. Astron. Soc.*, 445, 4161
- Hoyle F., Lyttleton R., 1941, *Mon. Not. R. Astron. Soc.*, 101, 227
- Hudson D., Mittal R., Reiprich T., Nulsen P., Andernach H., Sarazin C., 2010, *Astron. Astrophys.*, 513, A37
- Jacob S., Pfrommer C., 2017, *Mon. Not. R. Astron. Soc.*, 467, 1478
- Johnson A. R., Rudnick L., Jones T. W., Mendygral P. J., Dolag K., 2020, *Astrophys. J.*, 888, 101
- Jones C., Forman W., Vrtilik J., Sun M., O'Sullivan E., David L. P., 2017, *Astrophys. J.*, 842, 84
- Kennicutt R. C., 1998, *Astrophys. J.*, 498, 541
- King A., 2016, *Mon. Not. R. Astron. Soc. Lett.*, 456, L109
- Lakhchaura K., et al., 2018, *Mon. Not. R. Astron. Soc.*, 481, 4472
- Li Y., Bryan G. L., 2014, *Astrophys. J.*, 789, 54
- Li Y., Bryan G. L., Ruszkowski M., Voit G. M., O'Shea B. W., Donahue M., 2015, *Astrophys. J.*, 811, 73
- Li Y., Ruszkowski M., Bryan G. L., 2017, *Astrophys. J.*, 847, 106
- Martizzi D., Quataert E., Faucher-Giguère C. A., Fielding D., 2019, *Mon. Not. R. Astron. Soc.*, 483, 2465
- Martz C. G., et al., 2020, *Astrophys. J.*, 897, 57
- Mathews W. G., Faltenbacher A., Brighenti F., 2006, *Astrophys. J.*, 638, 659
- McDonald M., et al., 2019, *Astrophys. J.*, 885, 63
- McNamara B. R., Nulsen P. E. J., 2012, *New J. Phys.*, 14, 40
- McNamara B. R., Rohanizadegan M., Nulsen P. E., 2011, *Astrophys. J.*, 727, 39
- McNamara B. R., Russell H. R., Nulsen P. E. J., Hogan M. T., Fabian A. C., Pulido F., Edge A. C., 2016, *Astrophys. J.*, 830, 1
- Mccourt M., Sharma P., Quataert E., Parrish I. J., 2012, *Mon. Not. R. Astron. Soc.*, 419, 3319
- Meece G. R., Voit G. M., O'Shea B. W., O'Shea B. W., O'Shea B. W., 2017, *Astrophys. J.*, 841, 133
- Mehrgan K., Thomas J., Saglia R., Mazzalay X., Erwin P., Bender R., Kluge M., Fabricius M., 2019, *Astrophys. J.*, 887, 195
- Mendygral P. J., Jones T. W., Dolag K., 2012, *Astrophys. J.*, 750, 166
- Mohapatra R., Federrath C., Sharma P., 2021, *Mon. Not. R. Astron. Soc.*, 500, 5072
- Morsony B. J., Heinz S., Brüggem M., Ruszkowski M., 2010, *Mon. Not. R. Astron. Soc.*, 407, 1277
- Müller A., et al., 2021, *Nat. Astron.*, 5, 159
- Murgia M., 2011, *Mem. della Soc. Astron. Ital.*, 82, 507
- Newman W. I., Newman A. L., Rephaeli Y., 2002, *Astrophys. J.*, 575, 755
- Nixon C., King A., 2013, *Astrophys. J. Lett.*, 765, L7
- Nulsen P. E. J., David L. P., McNamara B. R., Jones C., Forman W. R., Wise M., 2002, *Astrophys. J.*, 568, 163
- Olivares V., et al., 2019, *Astron. Astrophys.*, 631, A22
- Pakmor R., Springel V., 2013, *Mon. Not. R. Astron. Soc.*, 432, 176
- Pakmor R. R. R., Bauer A., Springel V., 2011, *Mon. Not. R. Astron. Soc.*, 418, 1392
- Pakmor R., Springel V., Bauer A., Mocz P., Munoz D. J., Ohlmann S. T., Schaal K., Zhu C., 2016, *Mon. Not. R. Astron. Soc.*, 455, 1134
- Pakmor R., et al., 2017, *Mon. Not. R. Astron. Soc.*, 469, 3185
- Pakmor R., Guillet T., Pfrommer C., Gómez F. A., Grand R. J. J., Marinacci F., Simpson C. M., Springel V., 2018, *MNRAS*, 481, 4410
- Pakmor R., et al., 2020, *MNRAS*, 498, 3125
- Peterson J. R., Fabian A. C., 2006, *Phys. Rep.*, 427, 1
- Pfrommer C., 2013, *Astrophys. J.*, 779, 10
- Pfrommer C., Enßlin T. A., Sarazin C. L., 2005, *Astron. Astrophys.*, 430, 799
- Pfrommer C., Chang P., Broderick A. E., 2012, *Astrophys. J.*, 752, 24
- Pfrommer C., Werhahn M., Pakmor R., Girichidis P., Simpson C. M., 2022, *MNRAS*, 515, 4229
- Pillepich A., et al., 2018, *Mon. Not. R. Astron. Soc.*, 473, 4077
- Pizzolato F., Soker N., 2005, *ApJ*, 632, 821
- Powell K. G., Roe P. L., Linde T. J., Gombosi T. I., De Zeeuw D. L., 1999, *J. Comput. Phys.*, 154, 284
- Prasad D., Sharma P., Babul A., 2015, *Astrophys. J.*, 811, 108
- Prasad D., Sharma P., Babul A., 2018, *Astrophys. J.*, 863, 62
- Prasad D., Voit G. M., O'Shea B. W., Glines F., 2020, *Astrophys. J.*, 905, 50
- Pulido F. A., et al., 2018, *Astrophys. J.*, 853, 177
- Rafferty D. A., McNamara B. R., Nulsen P. E. J., Wise M. W., 2006, *Astrophys. J.*, 652, 216
- Russell H. R., Fabian A. C., McNamara B. R., Broderick A. E., 2015, *Mon. Not. R. Astron. Soc.*, 451, 588
- Russell H. R., et al., 2016, *Mon. Not. R. Astron. Soc.*, 458, 3134
- Russell H. R., et al., 2017, *Mon. Not. R. Astron. Soc.*, 472, 4024
- Russell H. R., Fabian A. C., McNamara B. R., Miller J. M., Nulsen P. E. J., Piotrowska J. M., Reynolds C. S., 2018, *Mon. Not. R. Astron. Soc.*, 477, 3583
- Russell H. R., et al., 2019, *Mon. Not. R. Astron. Soc.*, 490, 3025
- Ruszkowski M., Enßlin T. A., Brüggem M., Heinz S., Pfrommer C., 2007, *Mon. Not. R. Astron. Soc.*, 378, 662
- Ruszkowski M., Yang H. Y. K., Reynolds C. S., 2017, *Astrophys. J.*, 844, 13
- Ruszkowski M., Yang H.-Y. Y. K., Reynolds C. S., 2018, *Astrophys. J.*, 858, 64
- Sanders J. S., Fabian A. C., 2007, *Mon. Not. R. Astron. Soc.*, 381, 1381
- Sani E., et al., 2018, *Front. Astron. Sp. Sci.*, 5, 1
- Scharwächter J., McGregor P. J., Dopita M. A., Beck T. L., 2013, *Mon. Not. R. Astron. Soc.*, 429, 2315
- Sharma P., Mccourt M., Quataert E., Parrish I. J., 2012, *Mon. Not. R. Astron. Soc.*, 420, 3174
- Shemmer O., Netzer H., Maiolino R., Oliva E., Croom S., Corbett E., di Fabrizio L., 2004, *Astrophys. J.*, 614, 547
- Sijacki D., Pfrommer C., Springel V., Enßlin T. A., 2008, *Mon. Not. R. Astron. Soc.*, 387, 1403
- Sparre M., Pfrommer C., Ehlert K., 2020, *Mon. Not. R. Astron. Soc.*, 499, 4261
- Springel V., 2010, *Mon. Not. R. Astron. Soc.*, 401, 791
- Springel V., Hernquist L., 2003, *Mon. Not. R. Astron. Soc.*, 339, 289

- Sternberg A., Soker N., 2008, *Mon. Not. R. Astron. Soc.*, 384, 1327
- Talbot R. Y., Bourne M. A., Sijacki D., Bourne M. A., Sijacki D., 2021, *Mon. Not. R. Astron. Soc.*, 504, 3619
- Tremblay G. R., et al., 2016, *Nature*, 534, 218
- Tremblay G. R., et al., 2018, *Astrophys. J.*, 865, 13
- Vacca V., Murgia M., Govoni F., Enßlin T., Oppermann N., Ferretti L., Giovannini G., Loi F., 2018, *Galaxies*, 6, 1
- Vogelsberger M., Genel S., Sijacki D., Torrey P., Springel V., Hernquist L., 2013, *Mon. Not. R. Astron. Soc.*, 436, 3031
- Voit G. M., 2021, *Astrophys. J. Lett.*, 908, L16
- Voit G. M., Donahue M., 2005, *Astrophys. J.*, 634, 955
- Voit G. M., Donahue M., 2015, *Astrophys. J. Lett.*, 799, 1
- Wang C., Li Y., Ruszkowski M., 2019, *Mon. Not. R. Astron. Soc.*, 482, 3576
- Wang C., Ruszkowski M., Yang H. Y. K., 2020, *Mon. Not. R. Astron. Soc.*, 493, 4065
- Wang C., Ruszkowski M., Pfrommer C., Peng Oh S., Yang H. Y. K. Y. K., Oh S. P., Yang H. Y. K. Y. K., 2021, *Mon. Not. R. Astron. Soc.*, 504, 898
- Weinberger R., Ehlert K., Pfrommer C., Pakmor R., Springel V., 2017, *Mon. Not. R. Astron. Soc.*, 470, 4530
- Werner N., Urban O., Simionescu A., Allen S. W., 2013, *Nature*, 502, 656
- Wilman R. J., Edge A. C., Johnstone R. M., 2005, *Mon. Not. R. Astron. Soc.*, 359, 755
- Yang H.-Y. K., Reynolds C. S., 2016, *Astrophys. J.*, 829, 90
- Yang H.-Y. K., Reynolds C. S., Yang H.-Y. K., Reynolds C. S., 2016, *Astrophys. J.*, 818, 181
- Zhang C., Zhuravleva I., Gendron-Marsolais M.-L., Churazov E., Schekochihin A. A., Forman W. R., 2022, Prepr. (arXiv2203.04259)

APPENDIX A: MODEL PARAMETERS

To assess the relevance of parameter choices governing jet efficiency, we varied both ϵ and η independently. However, we find that only their product $\epsilon \times \eta$, which we refer to as *jet efficiency*, gives significant differences in the cluster evolution. In Fig. A1, we report on the evolution of the cold gas mass (with $T < 10^6$ K), SFR, jet luminosity L_{jet} and SMBH mass M_{bh} for runs with $\epsilon \times \eta = 0.001$ (red) and $\epsilon \times \eta = 0.0001$ (blue).

Runs with increased jet efficiency (reddish colours) in general show greater intermittency in star formation and jet power. More efficient jets pump more energy into the surrounding medium and halt cooling on longer timescales. Therefore, lower SFRs are observed. In addition, an increased injection of momentum forces cold gas on larger orbits around the center so that the accretion region is temporarily devoid of cold gas even though it remains present in the cluster (see Fig. A2).

On the other hand, lower jet efficiencies (bluish colours) lead to the formation of cold gas that is more closely tied to the center and is depleted at a constant *maximum* rate. Jet feedback is more continuous and less time-variable, while the high efficiency runs show higher burst powers and intermittent states of inactivity. Only the run with $\epsilon = 0.01$, $\eta = 0.01$, shows any significant variance after $t > 500$ Myr as a massive disc forms at $t \sim 1$ Gyr that is funneled into the accretion region on short timescales. Cooling is more significantly halted in the overheated cluster compared to its analogues at the same jet efficiency.

APPENDIX B: RESOLUTION

In agreement with our findings for the HD model, the high resolution analogue HDHR also forms a massive disc at $t \sim 1000$ Myr, which is accreted within $\Delta t \sim 800$ Myr (see Fig. B1). Hence, this demonstrates numerical convergence of the main properties of our hydrodynamic simulations. Throughout the simulation HDHR, the jet injects energy with $L_{\text{jet}} > 10^{45}$ erg s $^{-1}$, which is significantly more than in any other run. This leads to an overheated core so that no further cooling is triggered until $t = 2$ Gyr. We attribute this behavior to incomplete coupling with the hot and cold phases. As established earlier, magnetic fields are required to inhibit uncontrolled disc formation, we therefore omit the run from the following analysis.

In Fig. B2, we show our **Fiducial** model at the fiducial resolution. Compared to the high resolution analogue shown in Fig. B2, the general features are retained. Low-density bubbles rise that are deflected by cold gas in the ICM. Cavities are clearly discernible in X-ray emissivity.

In Fig. B3, we show the cold gas mass (M_{cold} with $T < 10^6$ K), SFR, jet luminosity (L_{jet}) and SMBH mass (M_{bh}). The evolution of the cold gas mass, star formation and jet power at high resolution are in general agreement with the low resolution counterparts. However, **BondiHR** forms a disc at $t \sim 1$, Gyr, which has vanished 500 Myr later. The related increased star formation and elevated jet power due to constant feeding leads to a somewhat distinct development. However, continued cooling quickly restores its earlier state of intermittent jet power and star formation as observed in **Bondi**. Similarly, the model **HR** shows a sudden increase in jet power at $t \sim 1750$ Myr probably due to accumulation of cold gas in the accretion region, which leads to a sudden spike in SMBH growth. We conclude that simulation-to-simulation variance appears more significant than resolution effects.

This paper has been typeset from a $\text{\TeX}/\text{\LaTeX}$ file prepared by the author.

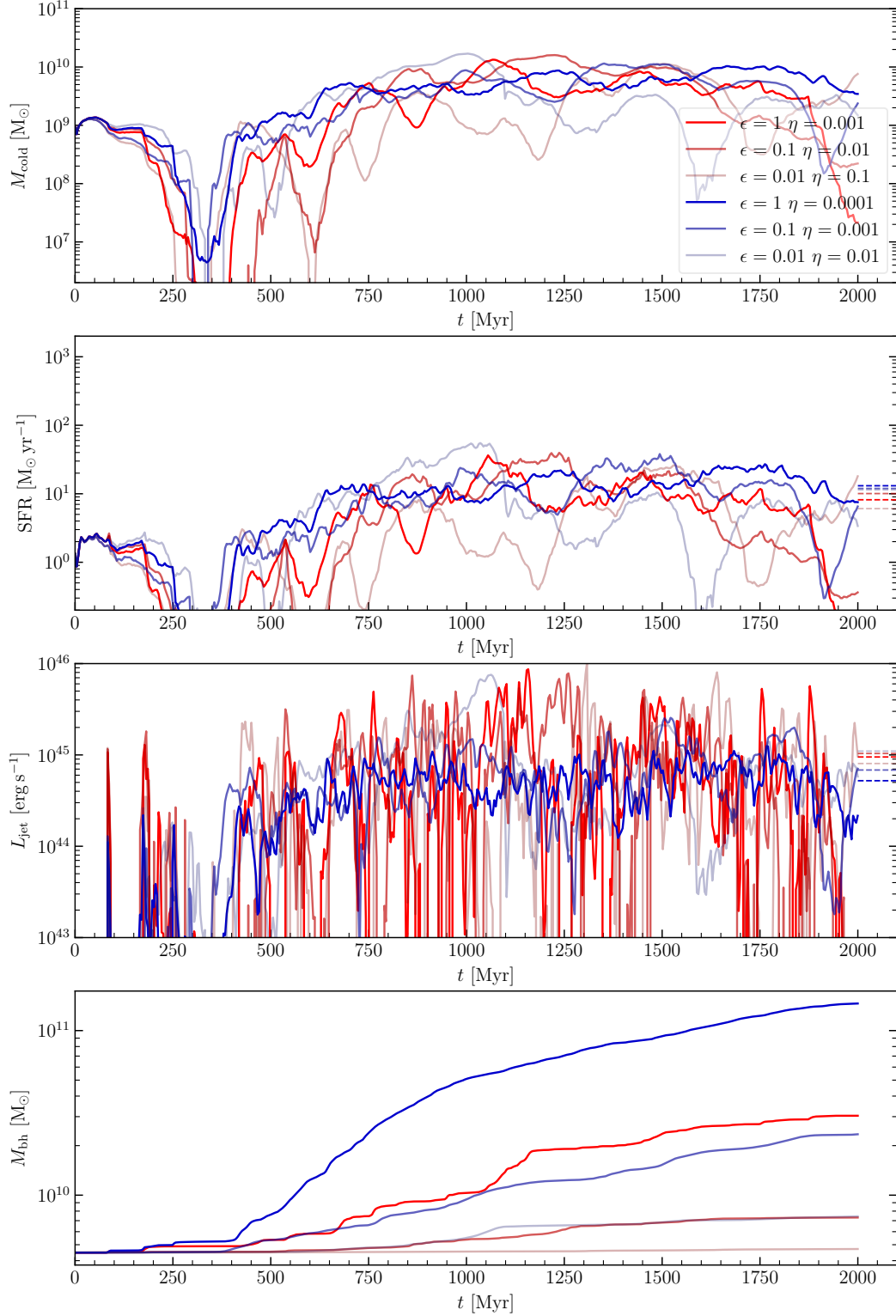


Figure A1. Same as in Fig. 6 for runs with varying parameters of the cold accretion model. Analogously, all models attain to a state of self-regulation with very similar average SFRs ($\text{SFR} \sim 10 M_{\odot} \text{yr}^{-1}$) and jet powers ($L_{\text{jet}} \sim 10^{45} \text{erg s}^{-1}$). Red and blue color shadings correspond to runs with $\epsilon \times \eta = 0.001$ and $\epsilon \times \eta = 0.0001$, respectively. Runs with lower coupling efficiencies show almost constant jet powers and SFRs while higher efficiencies cause star formation and jet powers to become more intermittent.

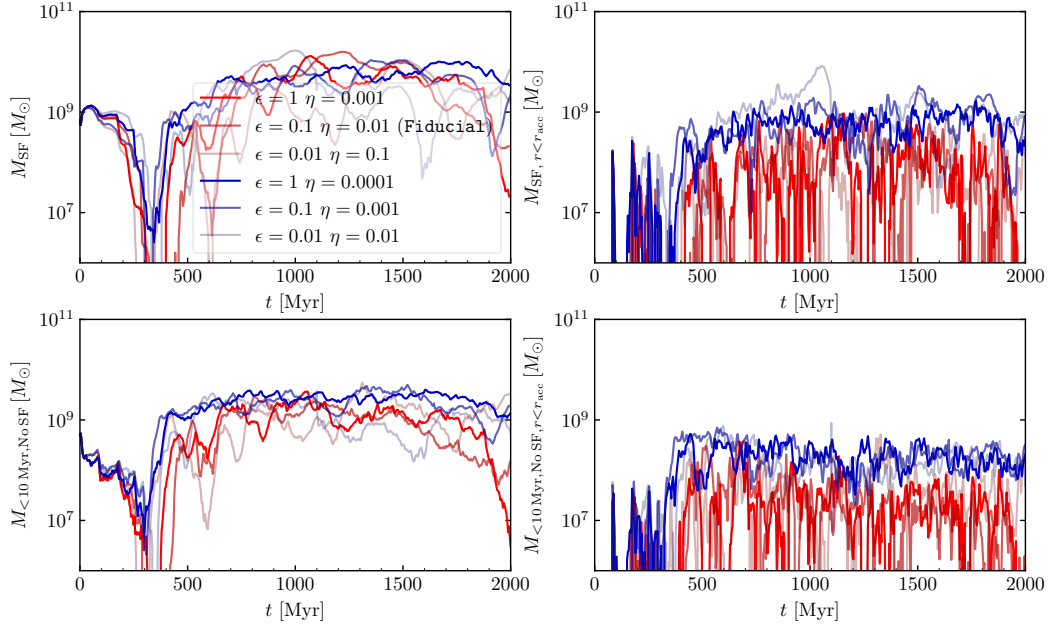


Figure A2. Same as in Fig. 8 for runs with varying parameters of the cold accretion model. Red and blue color shadings correspond to runs with $\epsilon \times \eta = 0.001$ and $\epsilon \times \eta = 0.0001$, respectively. Runs with lower efficiencies have a constant supply of cold gas that keeps powering the jets. More intermittent fluctuations are seen in the high efficiency runs. However, total cold and star forming gas masses stay within an order of magnitude.

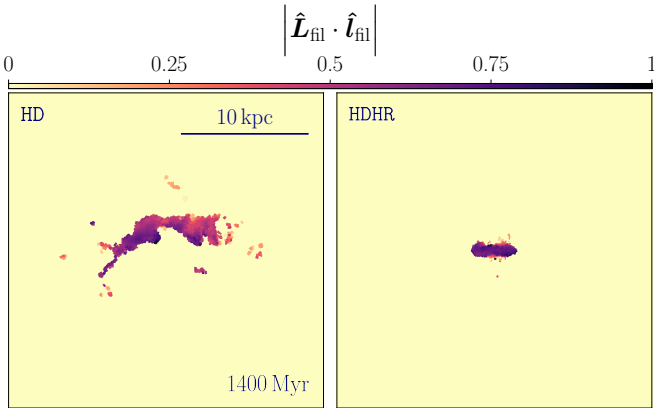


Figure B1. Same as in Fig. 12 for HD and HDHR at 1400 Myr. Both hydrodynamical runs form a strong disc at the end of the run. In HDHR the disc is funneled into the SMBH completely depleting the entire cold gas reservoir in the cluster.

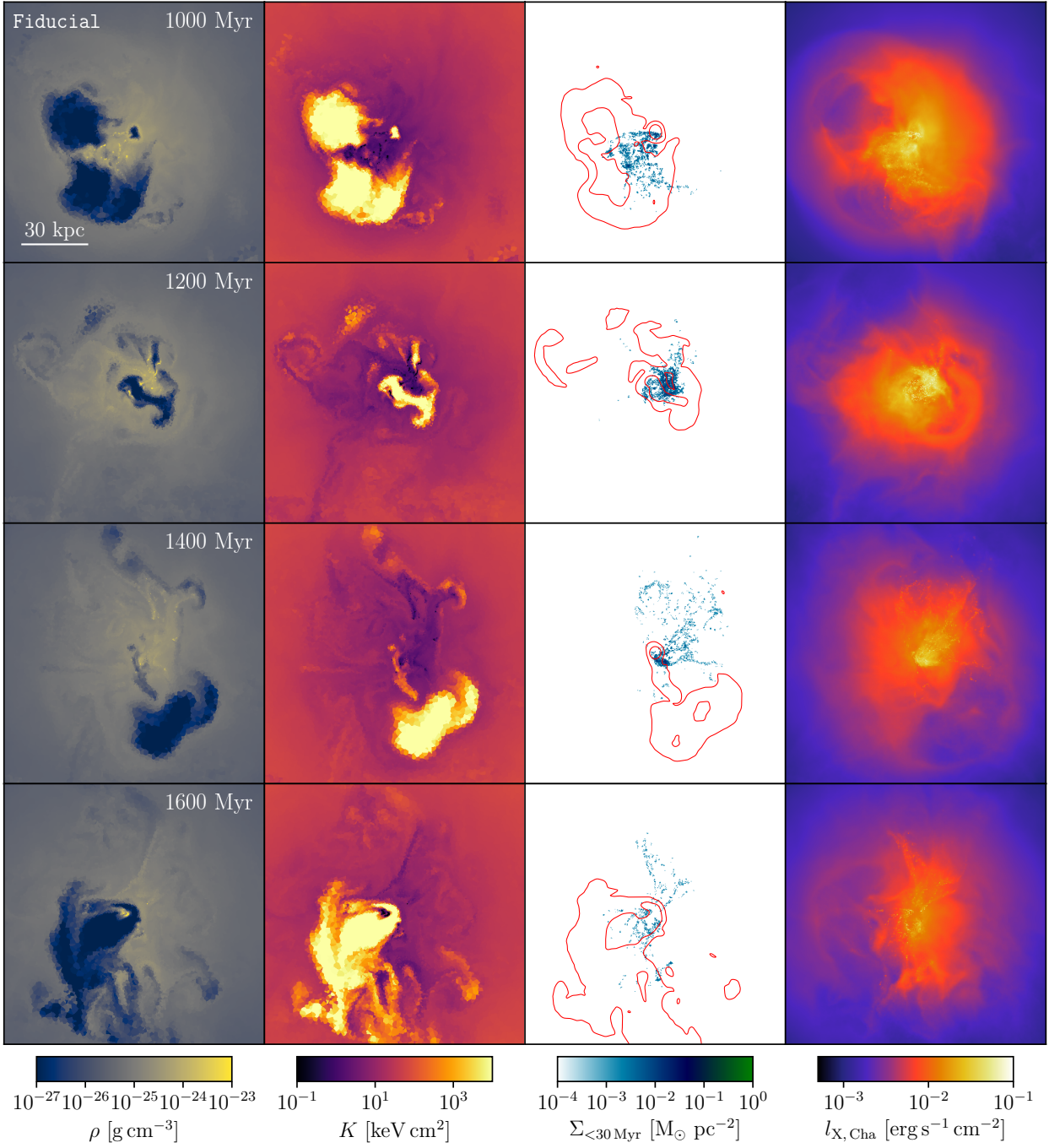


Figure B2. Same as in Fig. 3 for the same run at fiducial resolution **Fiducial**. The main features are independent of resolution.

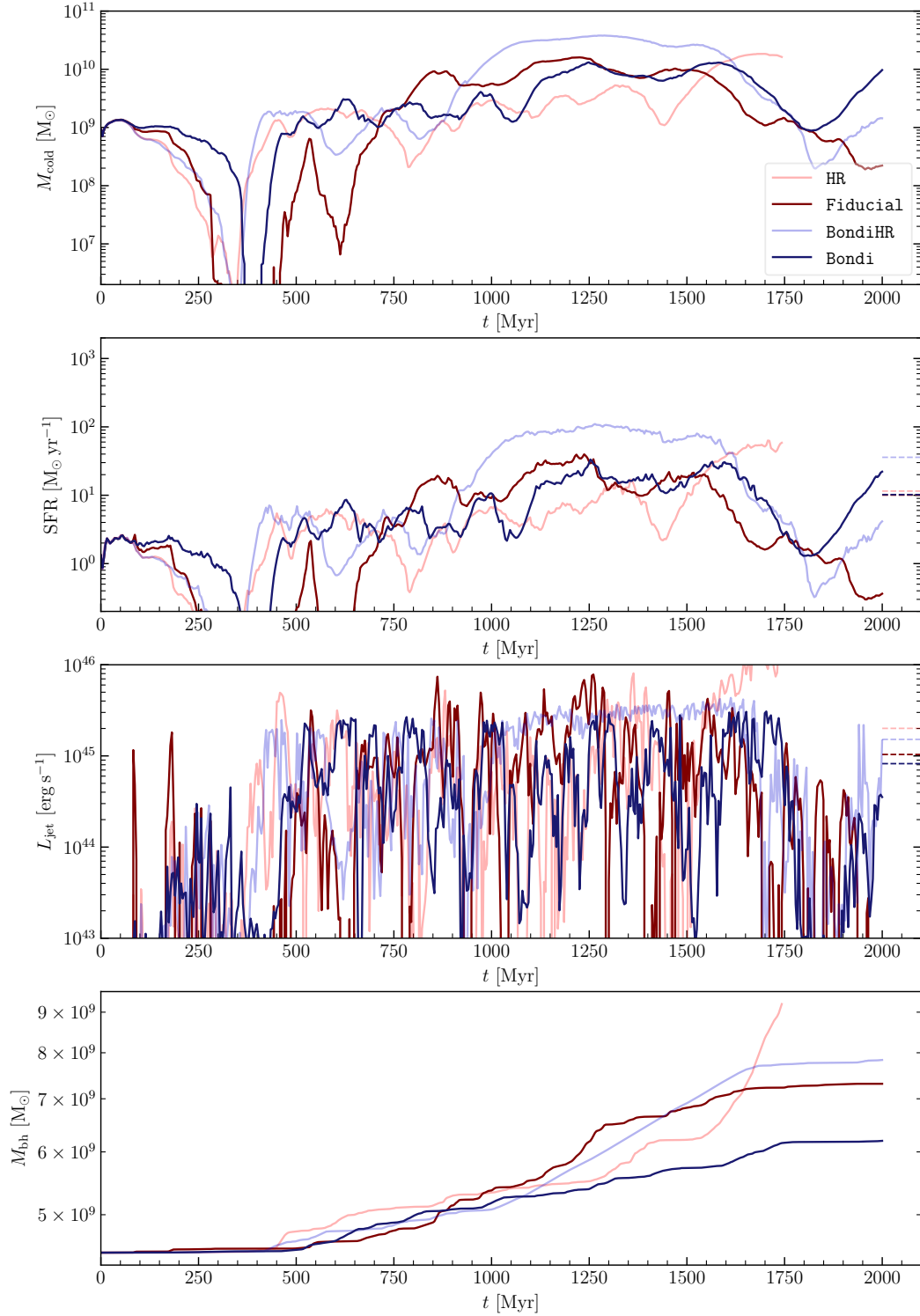


Figure B3. Same as in Fig. 6 for fiducial cold accretion and Bondi runs at varying numerical resolution. The cold accretion run gives very similar results at both resolutions. During the high resolution Bondi run a transient disc is formed with high SFRs ($\text{SFR} \sim 100 M_{\odot} \text{ yr}^{-1}$). The reason for its formation should probably be attributed to a chance event rather than the difference in resolution as varying parameters may also lead to the formation of transient discs.